

COMPUTATIONAL STUDIES OF THE FLOW AROUND  
ROUNDED AND DUCTED TIP HYDROFOILS

By

Hildur Ingvarsdóttir

B.Sc., University of Iceland, 1999

A THESIS SUBMITTED IN PARTIAL FULFILLMENT OF  
THE REQUIREMENTS FOR THE DEGREE OF  
MASTER OF APPLIED SCIENCE

in

THE FACULTY OF GRADUATE STUDIES  
DEPARTMENT OF MECHANICAL ENGINEERING

We accept this thesis as conforming  
to the required standard

THE UNIVERSITY OF BRITISH COLUMBIA

October 2001

© Hildur Ingvarsdóttir, 2001

In presenting this thesis in partial fulfilment of the requirements for an advanced degree at the University of British Columbia, I agree that the Library shall make it freely available for reference and study. I further agree that permission for extensive copying of this thesis for scholarly purposes may be granted by the head of my department or by his or her representatives. It is understood that copying or publication of this thesis for financial gain shall not be allowed without my written permission.

Department of Mechanical Engineering

The University of British Columbia  
Vancouver, Canada

Date Oct 9<sup>th</sup> 2001

## ABSTRACT

All lifting surfaces that terminate in a moving fluid create tip vortices. Tip vortices on marine propellers reduce the efficiency of the blades and can cause cavitation. Cavitation is an undesirable effect since it can cause pitting and erosion of the propeller and surrounding equipment and is a source of vibration and noise. Several tip devices have been proposed to suppress the tip vortex roll-up and reduce the strength of the tip vortices. One of those is a flow-through duct installed at the tip of a propeller blade.

In this research the flow over ducted and rounded tip hydrofoils was studied using the finite-volume flow solver CFD-ACE(U) and a  $k-\epsilon$  turbulence model. First the flow over two rounded tip hydrofoils, which were selected based on experimental data available, was studied with validation in mind. It was shown that away from the tip of the hydrofoil the sectional lift was predicted within 2% of experimental data whereas close to the tip the difference in lift reached up to 12%. The spanwise location of the vortex core was shown to be well predicted. This study was followed by studying the flow over a ducted tip hydrofoil. For comparative purposes a rounded tip hydrofoil of the same cross-section and aspect ratio run under the same flow conditions was studied. A good agreement in flow pattern was achieved between the computational results and available experimental data. A good agreement was also achieved between the maximum axial and tangential velocity immediately downstream of the hydrofoil. The computations showed that the ducted tip hydrofoil sheds less bound circulation over the majority of the wing span than does the rounded tip hydrofoil. The tip vortex from the ducted tip hydrofoil is shed in the shape of a duct instead of a concentrated circular vortex from the rounded tip hydrofoil.

# TABLE OF CONTENTS

<b>ABSTRACT.....</b>	<b>ii</b>
<b>TABLE OF CONTENTS .....</b>	<b>iii</b>
<b>LIST OF TABLES .....</b>	<b>v</b>
<b>LIST OF FIGURES .....</b>	<b>vi</b>
<b>NOMENCLATURE.....</b>	<b>ix</b>
<b>ACKNOWLEDGEMENT.....</b>	<b>x</b>
<b>CHAPTER 1 - INTRODUCTION.....</b>	<b>1</b>
1.1 Tip vortices .....	1
1.2 Previous Efforts to Alleviate the Effects of Tip Vortices.....	3
1.3 Previous Computational Studies of Tip Vortices .....	6
1.4 Scope of the Present Work and Structure of Thesis .....	7
<b>CHAPTER 2 - CFD MODELLING OF THE FLOW AROUND A DUCTED TIP HYDROFOIL.....</b>	<b>9</b>
2.1 Abstract.....	9
2.2 Introduction.....	9
2.3 Numerical implementation .....	12
2.4 Results.....	15
2.5 Conclusions.....	22

<b>CHAPTER 3 - COMPUTATIONAL STUDY OF THE FLOW AROUND A DUCTED TIP HYDROFOIL .....</b>	<b>24</b>
3.1 Abstract.....	24
3.2 Introduction.....	24
3.3 Numerical implementation .....	27
3.4 Results.....	34
3.5 Conclusions.....	48
<b>CHAPTER 4 - CONCLUSIONS AND RECOMMENDATIONS FOR FUTURE WORK .....</b>	<b>50</b>
4.1 Conclusions.....	50
4.2 Recommendations for Future Work .....	51
<b>REFERENCES.....</b>	<b>53</b>
<b>APPENDIX 1 - SIMULATION ON A 2D HYDROFOIL.....</b>	<b>55</b>
<b>APPENDIX 2 - SURFACE VECTOR PICTURES AND SFV PHOTOGRAPHS AT <math>\alpha = 7^\circ</math> .....</b>	<b>60</b>
<b>APPENDIX 3 - LIFT ON THE ROUNDED AND DUCTED TIP HYDROFOILS .....</b>	<b>63</b>

## LIST OF TABLES

Table 3.1	Comparison of Lift Coefficients ( $C_L$ ).....	37
Table A.1.1	Mesh Distribution for Convergence Study .....	56
Table A.1.2	Convergence Study - Lift and Drag Coefficients.....	57
Table A.3.1	Lift Coefficients for the Rounded and Ducted Tip Hydrofoils .....	63
Table A.3.2	Lift Coefficients for the Rounded and Ducted Tip Hydrofoils - Modified.....	63

## LIST OF FIGURES

Figure 1.1	Pressure field interpretation of tip vortices. ....	1
Figure 1.2	Helmholtz vortex theorem interpretation of tip vortices. (Source: Duan 1995) .....	2
Figure 1.3	Vorticity shed by a finite wing. (Source: Duan 1995) .....	2
Figure 2.1	The ducted tip propeller. ....	11
Figure 2.2	The 2D C-mesh is extruded along the foil in the z-direction to the plane opposite to the tip of the hydrofoil. ....	13
Figure 2.3	The surface mesh on the trailing edge and tip of the hydrofoil and a cut of the grid in the x-z plane. ....	14
Figure 2.4	Comparison of the chordwise pressure distribution at $z/s = 0.55$ for different density grids. ....	17
Figure 2.5	Comparison of the chordwise pressure distribution at $z/s = 0.971$ for different density grids. ....	17
Figure 2.6	The chordwise pressure distribution on the hydrofoil surface at $z/s = 0.676$ (measured from the root of hydrofoil) at $\alpha = 8^\circ$ and $Re = 2.9 \times 10^6$ . ....	18
Figure 2.7	The chordwise pressure distribution on the hydrofoil surface at $z/s = 0.971$ . ....	19
Figure 2.8	Pressure derived lift distribution over outer portion of wing. ....	19
Figure 2.9	The chordwise pressure distribution on the hydrofoil surface at $z/s = 0.667$ ( $y/s = 0.89$ ). ....	20
Figure 2.10	Total velocity magnitude across the vortex core at $x/c = 0.24$ aft of the trailing edge. ....	21
Figure 3.1	The ducted tip hydrofoil. ....	28
Figure 3.2	The 2D C-mesh is extruded along the foil in the z-direction to the plane opposite to the tip of the hydrofoil. ....	29
Figure 3.3	An example of a coarse surface mesh on the tip at the trailing edge of the hydrofoil and a cut of the grid in the x-z plane. ....	30

Figure 3.4	Blocks consisting of H-H meshes run through the duct and continue in the streamwise direction to the end of the flow domain. ....	31
Figure 3.5	Triangular gridding on hydrofoil tip and front of duct and formation of tetrahedral “capsule”. ....	32
Figure 3.6	Tetrahedral gridding in front of the duct. ....	32
Figure 3.7	The top and bottom sides of the “capsule” are also gridded with an H mesh which matches up with the surface mesh on the hydrofoil. ....	33
Figure 3.8	Grid topology for the ducted tip hydrofoil. ....	33
Figure 3.9	Comparison of inboard flow angles at trailing edge, suction side at $\alpha = 7^\circ$ . Refer to Figure 3.12 (a) for the definition of $\Phi$ . ....	36
Figure 3.10	Comparison of inboard flow angles at trailing edge, pressure side at $\alpha = 7^\circ$ . ....	36
Figure 3.11	Comparison of downwash flow angles at the tip at $\alpha = 7^\circ$ . Refer to Figure 3.12 (b) for the definition of $\epsilon$ . ....	37
Figure 3.12	Surface vector pictures of the (a) suction side, (b) tip and (c) pressure side and SFV photographs of the (d) suction side, (e) tip and (f) pressure side of the rounded tip hydrofoil at $\alpha = 12^\circ$ . ....	40
Figure 3.13	Surface vector pictures of the (a) suction side, (b) tip and (c) pressure side and SFV photographs of the (d) suction side, (e) tip and (f) pressure side of the ducted tip hydrofoil at $\alpha = 12^\circ$ . ....	41
Figure 3.14	Inboard flow angles at the trailing edge on the suction side at $\alpha = 7^\circ$ . ....	42
Figure 3.15	Inboard flow angles at the trailing edge on the suction side at $\alpha = 12^\circ$ . ....	42
Figure 3.16	Inboard flow angles at the trailing edge on the pressure side at $\alpha = 7^\circ$ . ....	43
Figure 3.17	Inboard flow angles at the trailing edge on the pressure side at $\alpha = 12^\circ$ . ....	43
Figure 3.18	Downwash flow angles at the tip at $\alpha = 7^\circ$ . ....	44
Figure 3.19	Downwash flow angles at the tip at $\alpha = 12^\circ$ . ....	44
Figure 3.20	The x-component of vorticity in the x-z plane right behind the trailing edge ( $x/c = 1.05$ ) of the (a) rounded tip and (b) ducted tip hydrofoil at $\alpha = 12^\circ$ and $Re = 1.2 \times 10^6$ . ....	46

Figure 3.21	Sectional lift along spanwise stations of the hydrofoils at $\alpha = 12^\circ$ and $Re = 1.2 \times 10^6$ . .....	47
Figure A.1.1	Grid shape and boundary conditions for modeling of 2D hydrofoil. ....	56
Figure A.1.2	Lift coefficients as a function of angle of attack at $Re = 9.0 \times 10^6$ . ....	58
Figure A.1.3	Drag coefficients as a function of lift coefficient at $Re = 9.0 \times 10^6$ . ....	59
Figure A.2.1	Surface vector pictures of the (a) suction side, (b) tip and (c) pressure side of the rounded tip hydrofoil at $\alpha = 7^\circ$ . ....	61
Figure A.2.2	SFV photographs of the (a) suction side, (b) tip and (c) pressure side of the rounded tip hydrofoil at $\alpha = 7^\circ$ . ....	61
Figure A.2.3	Surface vector pictures of the (a) suction side, (b) tip and (c) pressure side of the ducted tip hydrofoil at $\alpha = 7^\circ$ . ....	62
Figure A.2.4	SFV photographs of the (a) suction side, (b) tip and (c) pressure side of the ducted tip hydrofoil at $\alpha = 7^\circ$ . ....	62
Figure A.3.1	Sectional lift along spanwise stations of the hydrofoils at $\alpha = 7^\circ$ . ....	64

## NOMENCLATURE

$c$	=	chord length
$C_D$	=	drag coefficient
$C_L$	=	lift coefficient
$C_p$	=	pressure coefficient
$s$	=	span
$Re$	=	Reynolds number
SFV	=	Surface Flow Visualization
$U$	=	flow velocity in x-direction (freestream direction)
$U_\infty$	=	local freestream velocity
$U_\theta$	=	tangential velocity around the vortex core
$ V $	=	total velocity magnitude
$\alpha$	=	angle of attack
$\varepsilon$	=	downwash flow angle at the tip
$\Phi$	=	inboard flow angle (refer to Figure 3.12)

## ACKNOWLEDGEMENTS

I would first and foremost like to express my gratitude to my supervisors, Dr. Sheldon I. Green and Dr. Carl Ollivier-Gooch, for their great guidance, support and patience during the past couple of years. I simply could not have wished for better supervisors.

Secondly I would like to thank: Sif Gylfadottir, my friend and physical therapist, for keeping my head functional during the last stages of the thesis writing; Agust Torfi Hauksson, for taking the M.A.Sc.-UBC ride with me; Michelle Straver, for several good laughs over the mysterious ways of CFD; and Charles Boivin and Dr. Kendal Bushe, for always being ready to answer any computational questions I had.

Last but not least I would like to express my sincere thanks to my husband Oli and our families for all their love, support and encouragement during my UBC years.

Funding for this research was provided by the Natural Sciences and Engineering Research Council of Canada.

# CHAPTER 1 - INTRODUCTION

## 1.1 Tip vortices

All lifting surfaces that terminate in a moving fluid create tip vortices as a by-product. The physical mechanism for generating lift on a lifting surface moving in a fluid is the existence of high pressure on the bottom surface and low pressure on the top surface. The net imbalance of the pressure distribution creates the lift. The flow near the tips of the surface tends to curl around the tips, being forced from the high-pressure region just underneath the tips to the low-pressure region just above the tips. This flow establishes a circulatory motion resulting in a tip vortex.

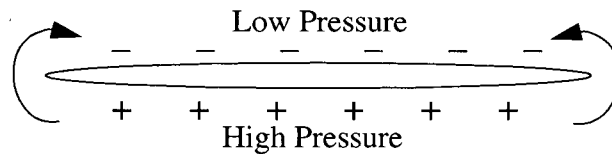


**Figure 1.1** Pressure field interpretation of tip vortices.

Another explanation of the existence of tip vortices derives from the application of Helmholtz vortex theorem. Consider a finite length wing impulsively started from rest. The difference in velocity between the pressure and suction surfaces of the wing implies a net circulation around the wing. Kelvin's Theorem demands that this circulation be matched by an equal and opposite shed circulation (the "starting vortex"). Helmholtz vortex theorem states that a vortex filament cannot end in a fluid; it must extend to the boundaries of the fluid or form a closed path. The two vortices must thus be connected by the so-called tip vortices.

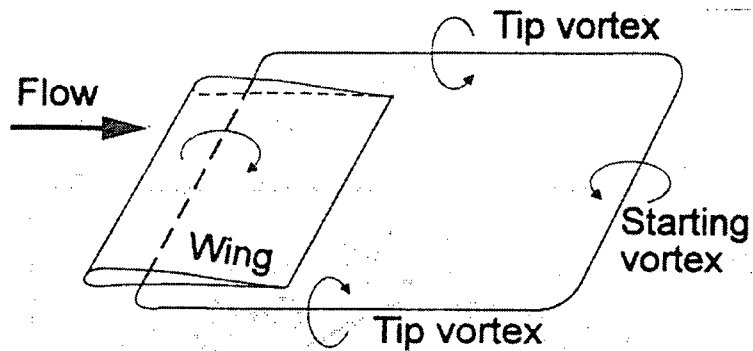


Figure 1.2 Helmholtz vortex theorem interpretation of tip vortices. (Source: Duan 1995)

A more realistic description of the development of tip vortices involves a number of lifting lines distributed along the span and chord of a wing as shown in Figure 1.3. As a result of this lifting line distribution, a sheet of vorticity is shed by the wing. This shed vorticity is unstable and rolls up due to its self-induced velocity field.

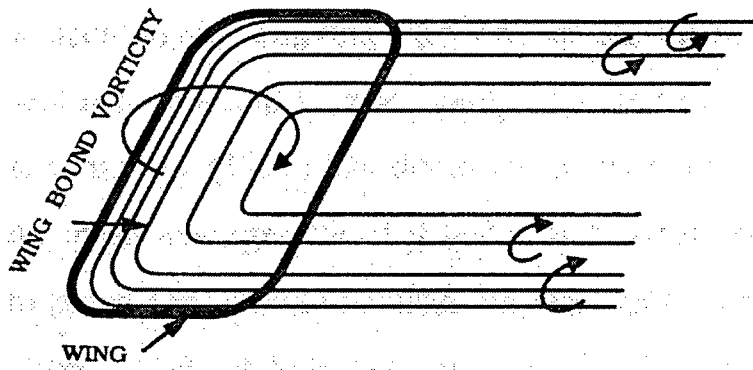


Figure 1.3 Vorticity shed by a finite wing. (Source: Duan 1995)

Tip vortices are of great importance because of their effect in several practical applications, such as landing separation distances for aircraft, blade/vortex interactions on helicopter blades, and propeller cavitation on ships. The application of interest here is propellers. Tip vortices on marine propellers have two undesirable effects: they reduce the efficiency of the blade and they may cause tip vortex cavitation. The reduction of efficiency is a result of the downward flow

component induced by the tip vortex. This is equivalent to the downwash on an airfoil, which both reduces the effective angle of attack and creates induced drag, thus resulting in efficiency reduction. High tangential velocities near the core of the tip vortex can reduce the local pressure causing cavitation. Tip vortex cavitation typically occurs well before blade and hub cavitation (Green et al. 1988, Kuiper 1978). Cavitation is an undesirable effect since it can cause pitting and erosion of the propeller and surrounding equipment and is also a source of vibration and noise.

## **1.2 Previous Efforts to Alleviate the Effects of Tip Vortices**

Because of the concentration of vorticity near wing and propeller tips, devices to redistribute and interact with vorticity around the tips have been studied ever since the introduction of finite wing theory. Two types of devices will be discussed briefly here; devices in aerodynamic applications and devices on and around propellers. Blade/vortex interactions on helicopter blades have resulted in testing of devices for helicopters as well, but those will not be discussed here.

### ***1.2.1 Aerodynamic Applications***

Kroo (2001) provides a good review of tip devices on wings in the Annual Review of Fluid Dynamics. The devices discussed there all have the purpose of reducing lift-dependent drag. The most commonly known device and the one that has found most commercial application is the winglet (Whitcomb winglet), which consists of a short (about half a chord high) lifting surface mounted almost normal to the wing at the tip. Well-designed winglets can provide significant reductions in airplane drag, and have now been incorporated on aircraft ranging from sailplanes to business jets and large commercial planes. An optimal design of winglets depends very much on the details of the wing structure, and the drag reduction achieved, if any at all, thus varies, but is normally on the order of 1% to 2%. Several variants of the winglet exist such as the

tip fence, which has been shown to reduce aircraft drag by 1.5% on some Airbus aircraft; tip sails, which appear less effective than a single vertical winglet with the same total span; and vortex diffusers. Rotating systems, such as propellers and turbines at the tips of wings, have been studied as well, but Kroo suggests there is no advantage of such devices over winglets or span extensions.

### ***1.2.2 Propeller Applications***

The most commonly used means to reduce the effects of tip vortices on propellers is the Kort Nozzle. The Kort nozzle consists of a duct that is fitted with a small clearance around the propeller. It can improve the efficiency of highly loaded propellers up to 10% but has some negative attributes as well. The added wetted surface creates extra drag when less heavily loaded and there are some installation limits related to the available space and the strength of the hull (Hordnes and Green 1998).

Platzer and Souders (1979) wrote a comprehensive survey of the efforts to alleviate the effects of tip vortices on marine propellers prior to 1980. One of the most promising concepts discussed is the installation of bulbous tips on propeller blades (Crump, 1948). Crump tested two different propellers with different configurations of propeller diameter, bulb diameter, pitch and number of blades. As much as a 25% increase in free stream velocity at inception of cavitation was seen with the bulbous tips attached in some configurations, with little effect on the propeller efficiency. However, experiments on a hydrofoil with a bulbous tip performed by Johnson and Rutgeresson (1991) showed no delay of cavitation inception but rather an accelerating effect and a 15% increase in drag on the hydrofoil.

More recent research includes replacement of conventional propeller tips with porous tips. Mani et al. (1988) found that such replacement can substantially delay cavitation inception without affecting the hydrodynamic performance. Itoh et al. (1987) also found that cavitation incep-

tion could be delayed and the propeller efficiency increased by 1-4 % by installing small bladelets on a model propeller. These results contradicted the findings of Goodman and Breslin (1980) who in fact saw additional cavitation problems and reduction in efficiency by installing bladelets on a conventional outboard propeller. It is likely that the difference in bladelet geometries used is the reason for the different findings.

Methods to suppress tip vortex cavitation other than changing the tip geometry of the blade have been studied as well. Fruman and Aflalo (1989) found a 60% reduction in tip vortex cavitation inception index by injecting a dilute polymer solution from an orifice at the tip of a hydrofoil without affecting the hydrodynamics of the hydrofoil. This was further supported by experiments on a model propeller by Chahine et al. (1993). The reduction was attributed to a significant thickening of the vortex core caused by the viscoelasticity of the solution.

Green et al. proposed a ducted tip geometry for hydrofoils in 1988. A ducted tip geometry on a hydrofoil or propeller is one in which flow-through ducts, aligned approximately with the hydrofoil/blade chord, are affixed at the hydrofoil/blade tips. Water and wind tunnel tests of ducted tip hydrofoils showed that the flow-through ducts suppress the tip vortex roll-up, thus resulting in a substantial delay in the onset of tip vortex cavitation (Green and Duan, 1995). This comes with little change in the lift to drag ratio. The ducted tip was later tested on a propeller. Hordnes and Green (1998) conducted sea trials of a ducted tip propeller and a conventional one and found a 50% reduction in the cavitation inception index on the ducted tip propeller. This cavitation inhibition comes without efficiency penalties. The efficiency of the ducted tip propeller is in fact up to 6% higher than the efficiency of the conventional propeller (Hordnes and Green, 1998).

### 1.3 Previous Computational Studies of Tip Vortices

A number of computational studies of tip vortex flows have been done in the past two decades, both on hydrofoils and propellers. The focus, however, has primarily been on validating methods for prediction and advancing the understanding of tip-vortex formation in general, rather than showing effects of tip modifications on tip vortices. A very brief review of a few of the more relevant and recent studies in this field will be given here. This review is only meant to be an introduction to some of the more outstanding contributions to the field of computational tip vortex research to date.

Dacles-Mariani et al. (1995) have carried out interactively a computational and experimental study of the wing tip vortex in the near field using a full Navier-Stokes simulation, accompanied by the Baldwin-Barth turbulence model. They applied prescribed inflow and outflow boundary conditions from experimental data and found that a fifth-order accurate upwind-biased differencing of the convective terms was essential to reduce numerical dissipation enough to achieve reasonable agreement with measured vortex velocity profiles. They were able to predict the velocity distribution in the vortex core in the near field to within 3% of the corresponding experiment, but the core static pressure was underpredicted.

Hsiao and Pauley (1998) have studied numerically the steady-state tip vortex flow over a finite-span hydrofoil using the three-dimensional incompressible Navier-Stokes flow solver, INS3D\_UP and the Baldwin-Barth one-equation turbulence model. They were able to achieve good agreement in pressure distribution and oil flow pattern with experimental data. They were also able to accurately predict vertical and axial velocities of the tip vortex core within the near-field wake region. Far downstream, however, the computed flow field showed an over-diffusive error within the tip vortex core, predicting a larger vortex core than the experimental data and a

deficit in the axial velocity in the vortex core instead of the excess obtained experimentally. After validating their results with numerical data, several effects such as change in Reynolds number, angle of attack and the tip-vortex rollup were studied.

Hsiao and Pauley have continued their work and done a numerical computation of tip vortex flow generated by a marine propeller (Hsiao and Pauley, 1999). The general characteristics of the propeller flow were well predicted but the vortex core predicted by the numerical method used was overly diffusive and dissipative, despite using a fifth-order accurate scheme for the convective terms.

#### **1.4 Scope of the Present Work and Structure of Thesis**

The aim of this research is twofold:

- To expand our knowledge and understanding of the flow around a duct attached to the tip of a hydrofoil.
- To provide a good basis for computational optimization of the duct size, shape and location on a propeller blade.

The research is motivated and based on the results of Green and Duan (1995) and Hordnes and Green (1998). To do this, CFD software has been used to compute the flow over rounded and ducted tip hydrofoils.

This thesis has been written in research paper format. Chapter 2 is a paper describing a validation study on rounded tip hydrofoils which was presented at The Sixth Canadian Marine Hydromechanics and Structures Conference. Chapter 3 contains a second paper in which rounded and ducted tip hydrofoils are studied computationally. References for both those papers are found in one list of references including any other references used throughout the thesis. A Summary and Future Work are the topics of Chapter 4. Chapters 1-4 are followed by the list of references

and 3 appendices. Appendix 1 contains a validation study that was done on a two dimensional hydrofoil. The second appendix contains excess surface flow visualization results that are not presented in Chapter 3. Computational results for lift on rounded and ducted tip hydrofoils are presented in Appendix 3.

## **CHAPTER 2 - CFD MODELLING OF THE FLOW AROUND A DUCTED TIP HYDROFOIL**

This chapter was published as a paper in the Proceedings of The Sixth Canadian Marine Hydrodynamics and Structures Conference. The bibliographic reference for this paper is:

Ingvarsdottir, H., Ollivier-Gooch, C., and Green, S. I., 2001, "CFD Modelling of the Flow Around a Ducted Tip Hydrofoil," Proceedings of The Sixth Canadian Marine Hydromechanics and Structures Conference, Vancouver, Canada, pp. 55-60.

### **2.1 Abstract**

The flow over a finite-span hydrofoil has been studied using the finite-volume flow solver CFD-ACE(U) from CFD Research Corporation. The aim of the study was to provide a good basis for future modelling of ducted tip hydrofoils and a ducted tip propeller. A  $k-\epsilon$  turbulence model and a combination of C-H, H-H and prismatic grids were used to cover the flow domain. Cases were run with a second order accurate upwind differencing scheme using approximately 150,000 - 436,000 cells. Comparison with experimental data showed that away from the tip of the hydrofoil the pressure distribution was well predicted and sectional lift was predicted within 2% of experimental data whereas closer to the tip the difference in lift reached up to 12%. The total lift is in good agreement with lifting line theory. It was also shown that the spanwise location of the vortex core was well predicted. Future work will include developing a solid model of a hydrofoil with a ducted tip and running simulations for the flow around it. A final stage of the research will involve simulations and optimization of ducted tip propellers.

### **2.2 Introduction**

All lifting surfaces that terminate in a moving fluid create tip vortices. Tip vortices on marine propellers have two undesirable effects: they reduce the efficiency of the blade and they may

cause tip vortex cavitation. The latter typically occurs well before blade and hub cavitation. Cavitation is an undesirable effect since it can cause pitting and erosion of the propeller and surrounding equipment and is also a source of vibration and noise.

There are several devices that have been tried or are being used to reduce the effects of tip vortices. The most commonly used means is the Kort nozzle. The Kort nozzle has the form of a shaped duct that fits with a fairly small clearance around the propeller. Kort nozzles can improve the efficiency of highly loaded propellers by up to 10 percent but the added wetted surface creates extra drag, which implies a reduction in efficiency when the propeller is less heavily loaded (Hordnes and Green, 1998). Other devices that have been proposed to alleviate the effects of tip vortices include bulbous tips installed on propeller blades (Crump, 1948), porous blade tips (Mani et al., 1988) and fitting small bladelets to each propeller blade tip (Itoh et al., 1987).

A number of computational studies have been done on tip vortices, both in aerodynamic and marine applications. Two studies of the most relevance to the current work were done by Hsiao and Pauley (1998) and Dacles-Mariani et al. (1995). Hsiao and Pauley conducted a numerical study of the steady state tip vortex flow over a finite-span hydrofoil. They studied the effects of angle of attack, Reynolds number and the hydrofoil planform on the tip vortex. After obtaining a good agreement between the numerical pressure distribution along the hydrofoil and experimental data, they studied the roll-up of the tip vortex. Dacles-Mariani et al. (1995) carried out interactively a computational and experimental study of the wingtip vortex in the near field. They applied inflow and outflow boundary conditions from the experimental data and obtained good agreement between the computed and measured flowfields.

The particular wing geometry of interest in this study is one with a ducted tip. A ducted tip geometry on a hydrofoil or propeller is one in which flow-through ducts, aligned approximately

with the blade chord, are affixed at the blade tips. The ducted tip geometry was first proposed by Green et al. (1988). Water and wind tunnel tests of ducted tip hydrofoils have shown that the flow-through ducts suppress the tip vortex roll-up, thus resulting in a substantial delay in the onset of tip vortex cavitation (Green and Duan, 1995). Also, sea trials of a ducted tip propeller have been conducted. A study on two 4 bladed, 36 inch diameter (29 inch pitch) propellers, one conventional and one fitted with ducted tips, has shown that the cavitation inception index for the ducted tip propeller is 50% lower than that for the conventional propeller. This comes without efficiency penalties. The efficiency of the ducted tip propeller is in fact up to 6% higher than the efficiency of the conventional propeller (Hordnes and Green, 1998).

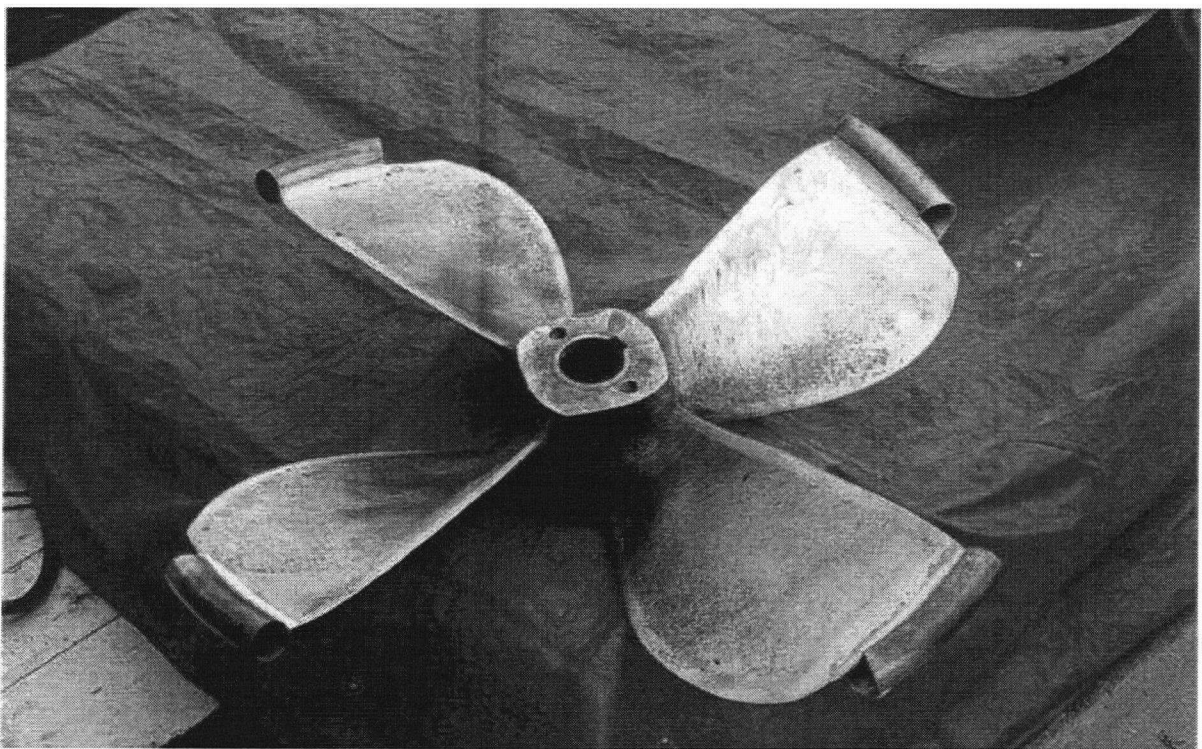


**Figure 2.1** The ducted tip propeller.

In the previous studies mentioned above, the ducted tip has been selected in a fairly ad hoc way, without a detailed understanding of the three-dimensional hydrodynamics around the duct. The aim of our study is to use a CFD model to optimize the shape and location of the ducted tip.

The CFD model of the propeller is being made in several steps. First a 2D hydrofoil is modelled followed by a 3D hydrofoil with a rounded tip. These cases are validated with experimental data. Next a 3D hydrofoil with a ducted tip will be studied and eventually a 3D propeller with ducted tips will be considered. In this paper, computational results for 3D hydrofoils with round tips are presented and compared to experimental data.

## **2.3 Numerical implementation**

The current study considers a steady flow past two hydrofoils with NACA 0012 and NACA 0015 airfoil sections. The hydrofoils, their computational domains, and the flow properties of the surrounding fluid have been chosen with comparison to available experimental data in mind. The NACA 0012 airfoil results are compared to the experimental results of Dacles-Mariani et al. (1995). The NACA 0015 airfoil results are compared to the experimental results of McAlister and Takahashi (1991). These different cases will be referred to as the Dacles-Mariani case and the McAlister case.

### ***2.3.1 Geometry and Grid Generation***

The NACA 0012 hydrofoil has an aspect ratio of 0.75 and the NACA 0015 hydrofoil has an aspect ratio of 3.3. Both aspect ratios are based on semispan and both hydrofoils have no twist or taper. The semispan is measured from the root of the foil to the quarter chord point on the round tip. The edge shape of the round tip of both foils is formed by rotating the two dimensional hydrofoil section around its camberline. Both foils are tilted around their quarter chord lines when run at an angle relative to the freestream flow.

Several grid generation methods have been explored in attempts to resolve the flow near the tip-vortex core and the hydrofoil surface. The multiblock grids that have been used for the study

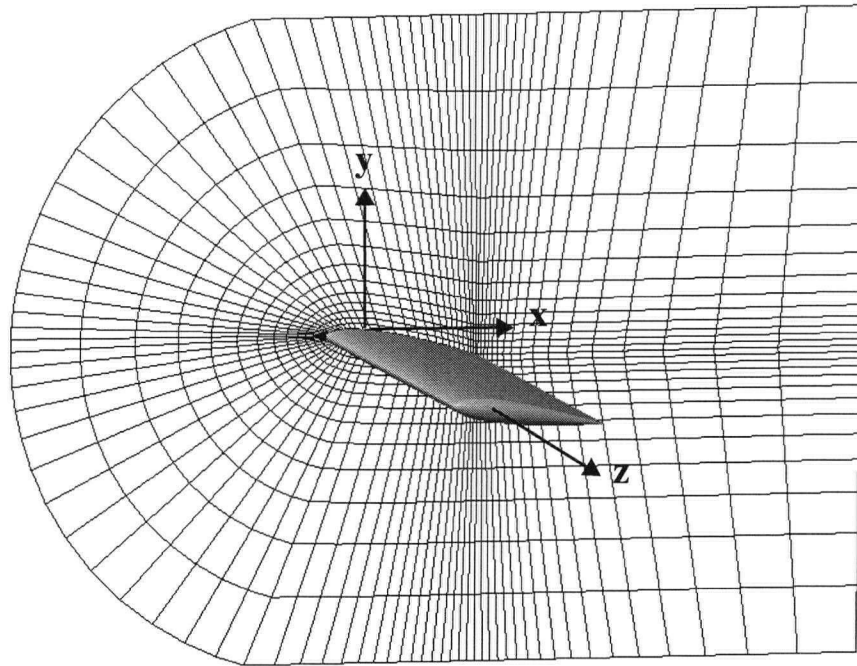


**Figure 2.2** The 2D C-mesh is extruded along the foil in the z-direction to the plane opposite to the tip of the hydrofoil.

presented here consist of both structured hexahedral and semistructured prismatic blocks. The grids have been generated with CFD-GEOM from CFD Research Corporation. A C-mesh has been wrapped around a two dimensional section of the hydrofoil and extruded along the foil from the symmetry plane to the opposite side of the domain to form a C-H mesh (Figure 2.2). The cavity formed between the tip of the foil and the opposite wall has been filled with an H-H mesh extending approximately from 3% of the chord length to 94% of the chord length of the hydrofoil. The leading and trailing edge parts of the tip have been gridded with a triangular surface grid, which has then been extruded across the domain forming a prismatic grid to match the C-H and H-H blocks (Figure 2.3). To avoid very skewed cells at the leading edge and high aspect ratio cells at the trailing edge tip, these regions were meshed prismatically.

The dimensions of the computational domains for the McAlister case and Dacles-Mariani case are as follows.

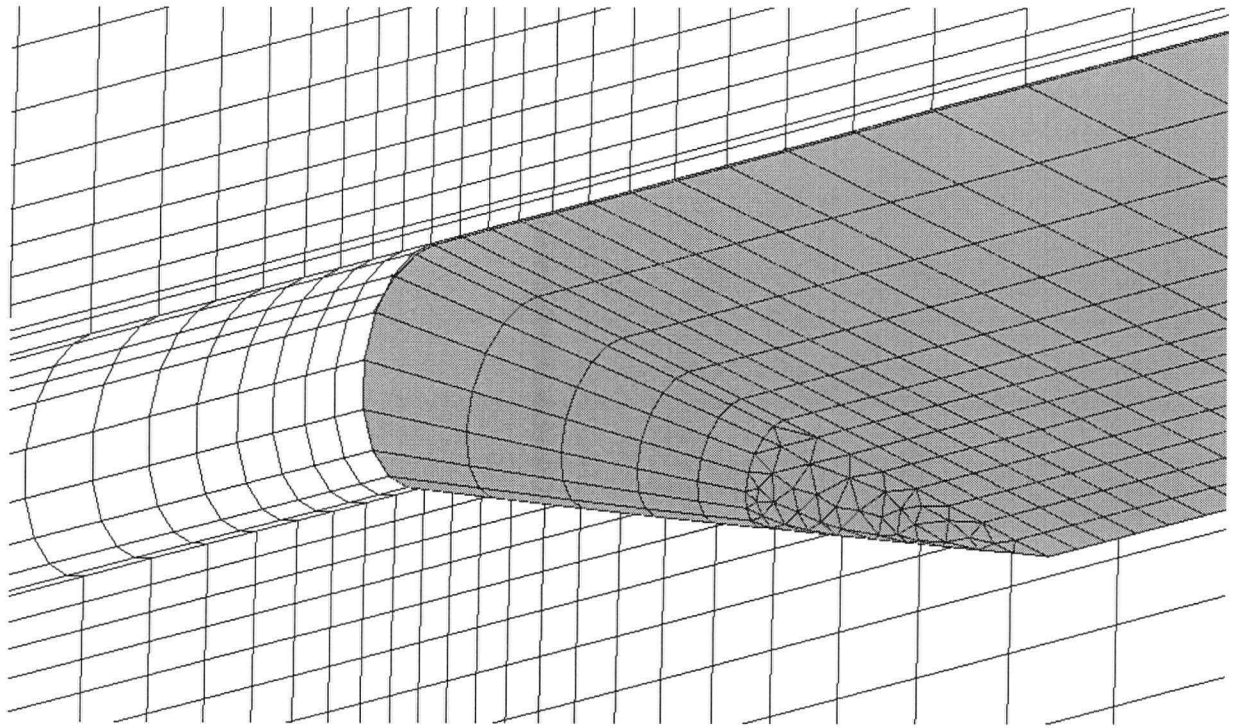


**Figure 2.3** The surface mesh on the trailing edge and tip of the hydrofoil and a cut of the grid in the x-z plane.

**McAlister Case.** The 3.3 aspect ratio hydrofoil is placed with its quarter chord line 3.5 chord lengths from the top and bottom symmetry planes. The domain is 5 chordlengths wide (spanwise). The domain extends 2.5 chordlengths downstream of the trailing edge and 2 chordlengths upstream of the leading edge.

**Dacles-Mariani Case.** The 0.75 aspect ratio hydrofoil is placed with its quarterchord line 0.33 chord lengths from the top and bottom symmetry planes. The domain is 1 chord length wide (spanwise). The domain extends 2 chord lengths downstream of the trailing edge and 2 chord lengths upstream of the leading edge. It should be noted that in order to provide an inlet sufficiently far upstream for the Dacles-Mariani domain, the front part of the C-H mesh (which only extended 0.3 chord lengths upstream from the leading edge) was matched with an H-H mesh to provide an inlet 2 chord lengths upstream of the leading edge.

### ***2.3.2 Numerical Method***

The pressure-based, finite-volume flow solver CFD-ACE(U) from CFDRC has been used in this study. The code uses unstructured/hybrid grids to integrate the Navier-Stokes equations. Cases have been run with a k- $\epsilon$  turbulence model and a second-order accurate upwind differencing scheme.

### ***2.3.3 Boundary Conditions***

Since each grid consists of multiple blocks, two types of boundary conditions have to be specified: 1) the physical boundaries such as inflow, outflow and walls and 2) the block-interface boundaries across which all flow quantities must be continuous.

For the physical boundaries, freestream velocity is specified for the inlet and constant pressure for the outlet. Other sides, corresponding to the walls of the tunnel being modelled, are specified as symmetry walls. On the solid hydrofoil surface, a no-slip flow condition is used.

## **2.4 Results**

Given that the aim of this study is to provide a good base for modelling the flow around a ducted tip hydrofoil and later the ducted tip propeller, the focus in this study has primarily been on grid dependence and validation of the numerical results with experimental data.

### ***2.4.1 Grid Dependence***

Grid dependence has been studied for the McAlister case. The primary grid used for the McAlister case in this study has a total of approximately 436,000 cells. The C-H grid has 159x35x77 grid points in the streamwise, surface-normal and spanwise directions, respectively. 101 of the 159 streamwise grid points and 43 of the 77 spanwise grid points are used on the hydrofoil. The first grid spacing on the hydrofoil surface is specified at 0.001 chord length above

the hydrofoil surface. The H-H grid extending from the midsection of the tip has 29x17x35 grid points and the nose and tail prism grids have 8092 and 4216 cells respectively.

The results obtained from the primary grid are compared with the results obtained from a 153,000 cell grid in Figure 2.4 and 2.5. The main difference in the two grids lies in the first cell spacing (0.004 chord length in the less dense grid) and a less resolved tip vortex both in the streamwise and spanwise directions. Figure 2.4 shows the surface pressure distribution close to the midspan of the hydrofoil obtained from the different grids. The dense grid causes negligible difference in the pressure on the pressure side on the hydrofoil. The primary difference can be seen in the pressure peak on the suction surface. The difference can be attributed to a better resolved mesh at the leading edge for the grid with more cells. Close to the tip there is more difference in the pressure distribution obtained from the two grids as is shown in Figure 2.5. As can be seen there is little difference in the pressure on the pressure side but a significant difference on the suction side, especially towards the trailing edge where the tip vortex starts to roll up. It is expected, and shown here, that greater resolution of the leading edge and the tip vortex region causes higher pressure peaks to be predicted.

#### ***2.4.2 Comparison with the experimental results of McAlister and Takahashi (1991)***

The primary computation conducted for comparison with McAlister's and Takahashi's data was done at Reynolds number  $Re = 2.9 \times 10^6$  (based on the chord length and the free stream velocity) and angle of attack  $\alpha = 8^\circ$ . Figures 2.6 and 2.7 show the surface pressure distribution at two different spanwise stations, away from and close to the tip. Away from the tip the agreement is generally quite good. The computed suction side pressure coefficient is slightly lower than McAlister and Takahashi's experimental data. It is likely that a greater number of grid points in the leading edge region will produce a better resolved suction peak. Close to the tip the agreement

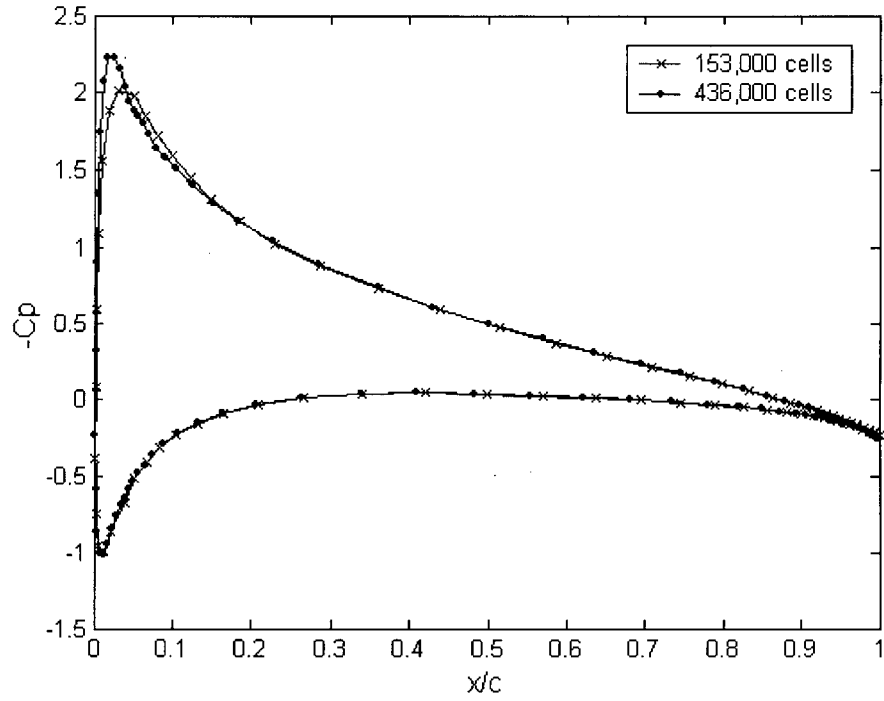


Figure 2.4 Comparison of the chordwise pressure distribution at  $z/s = 0.55$  for different density grids.

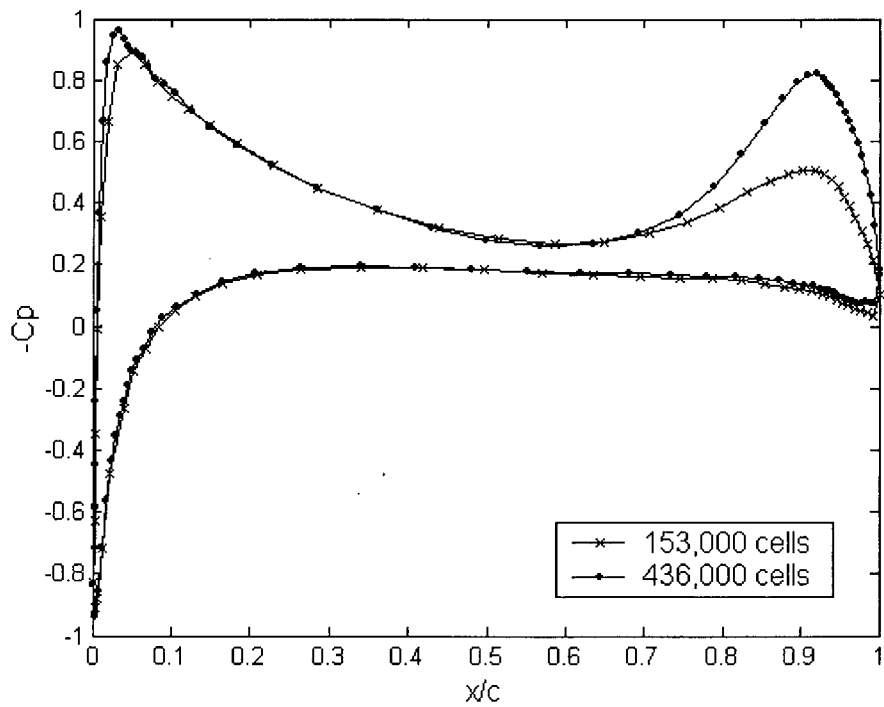
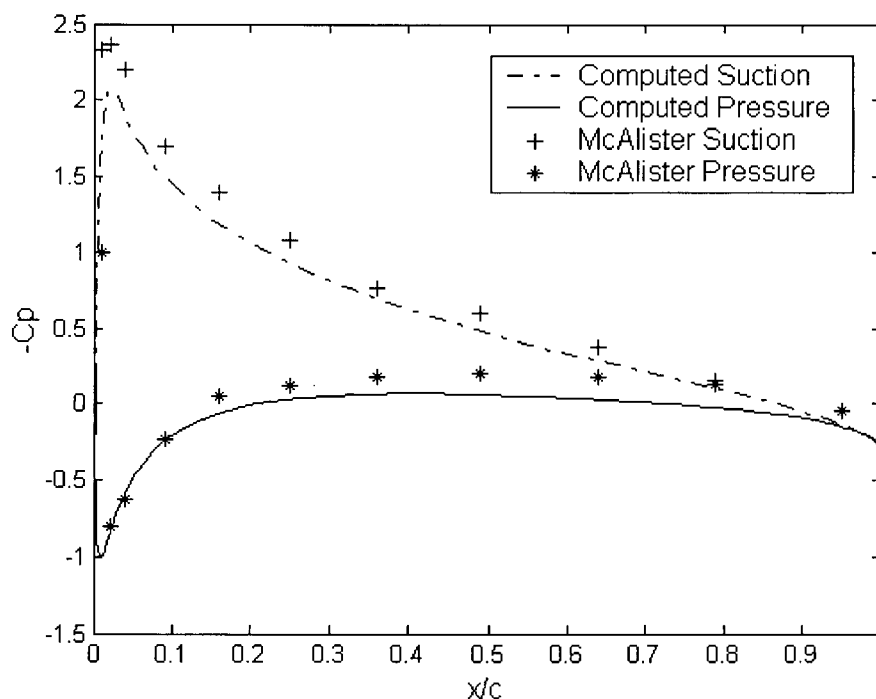


Figure 2.5 Comparison of the chordwise pressure distribution at  $z/s = 0.971$  for different density grids.

is worse. The pressure distribution towards the tip is determined by the details of the three dimensional tip vortex rollup and separation from the surface. It is likely that a combination of poor grid resolution and a low order accuracy scheme along with diffusion in the turbulence model cause the strength of the vortex to be under predicted. The agreement with experiments is generally good away from the tip and poorer close to the tip, which is consistent with the findings of Hsiao and Pauley (1998).



**Figure 2.6** The chordwise pressure distribution on the hydrofoil surface at  $z/s = 0.676$  (measured from the root of hydrofoil) at  $\alpha = 8^\circ$  and  $Re = 2.9 \times 10^6$ .

The pressure-derived lift distribution over the outer portion of the hydrofoil was computed and is compared to experimental data in Figure 2.8. Close to the tip the difference in experimental and computational lift coefficients is up to 0.07 whereas further away from the tip the difference is around 0.01-0.015. The computed total lift coefficient is 0.66, which compares well to a lift coefficient of 0.67 predicted by lifting line theory for a wing of the same aspect ratio.

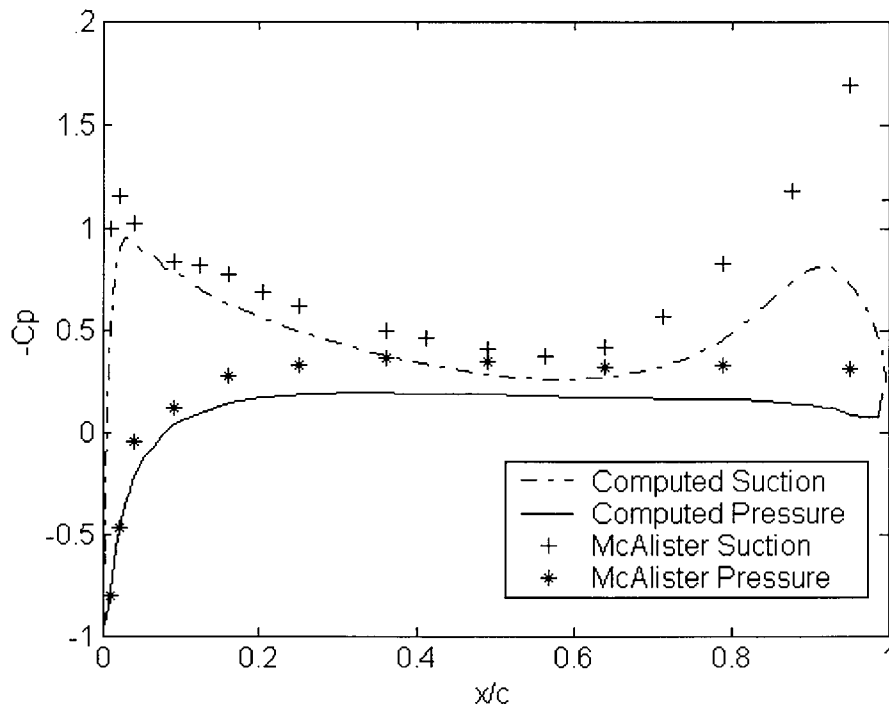


Figure 2.7 The chordwise pressure distribution on the hydrofoil surface at  $z/s = 0.971$ .

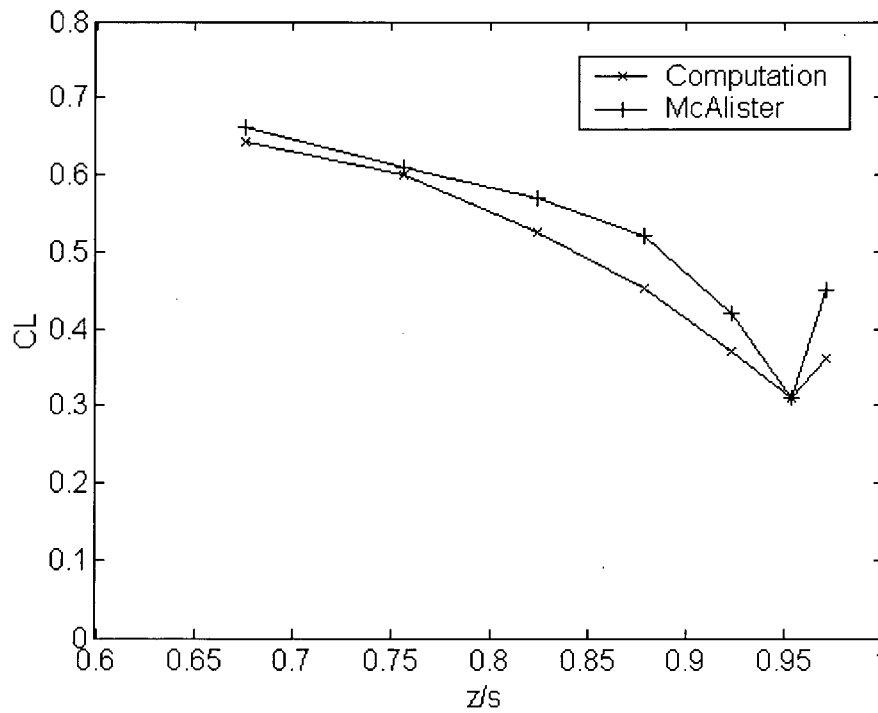


Figure 2.8 Pressure derived lift distribution over outer portion of the hydrofoil.

### 2.4.3 Comparison with the experimental results of Dacles-Mariani et al. (1995)

The primary computation conducted for comparison with the experimental data of Dacles-Mariani et al. was done at Reynolds number  $Re = 4.6 \times 10^6$  (based on the chord length and the free stream velocity) and angle of attack  $\alpha = 10$  degrees. The grid has around 207,000 cells with the first grid cell located at 0.0012 chord lengths above the hydrofoil surface. The C-H mesh has 145x25x51 grid points in the streamwise, surface-normal and spanwise directions, respectively. 97 of the 145 streamwise grid points and 32 of the 51 spanwise grid points are used on the hydrofoil. The inlet H-H mesh has 15x31x51 grid points and the H-H mesh along the tip of the foil has 30x15x20 grid points. The nose and tail prismatic grids have 2812 and 3040 cells respectively. Presented in Figure 2.9 is a comparison of the computed and experimental pressure distribution along the hydrofoil surface close to the tip (located roughly under the vortex). Although there are

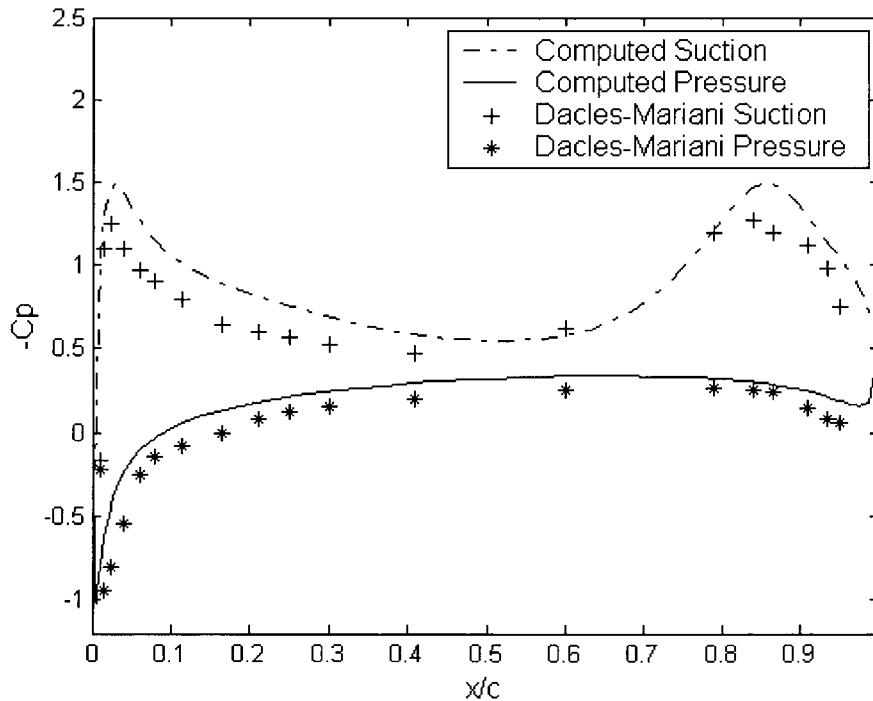
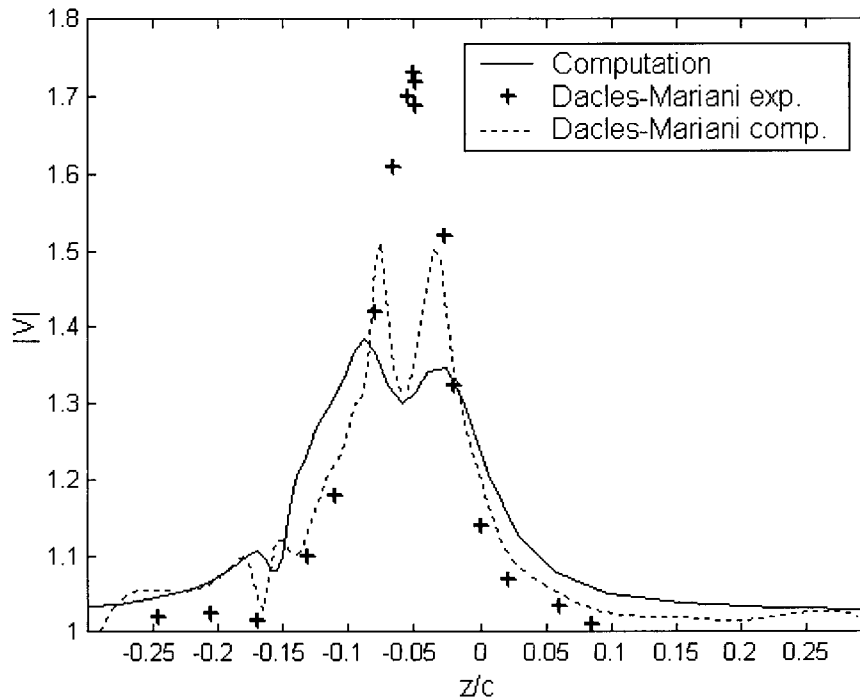


Figure 2.9 The chordwise pressure distribution on the hydrofoil surface at  $z/c = 0.667$  ( $z/s = 0.89$ ).



**Figure 2.10** Total velocity magnitude across the vortex core at  $x/c = 0.24$  aft of the trailing edge.

some differences, the plot indicates that the vortex-induced peak suction is captured reasonably well by this computation. Figure 2.10 shows the total velocity magnitude across the vortex core about a quarter chord behind the trailing edge. The agreement between the experimental and computed shapes of the velocity magnitude distribution indicates that the spanwise location of the vortex is predicted correctly. However, unlike the experimental measurements, the velocity does not reach a peak in the middle of the vortex core, but instead dips. The dip in the total velocity magnitude is likely caused by a combination of poor grid resolution around the vortex core and diffusion of the vortex by the turbulence model. Dacles-Mariani et al. observed a similar dip in the total velocity, even though they used a 5<sup>th</sup> order accurate upwind-biased differencing of the convective terms and a Baldwin-Barth turbulence model. Their results are shown in Figure 2.10 as well. By modifying the production term in the model to suppress excessive diffusion of the

vortex they were able to predict the velocity peak closer to the experimentally measured velocity peak (Dacles-Mariani et al., 1995). It should be noted that for the computation of the velocity magnitude in the vortex core, Dacles-Mariani et al. set computational flow conditions at the trailing edge to match experimental data.

## **2.5 Conclusions**

The flow over a finite-span hydrofoil has been studied using the finite-volume flow solver CFD-ACE(U) from CFDRC. A  $K-\epsilon$  turbulence model and a combination of C-H, H-H and prism grids were used. Cases were run with a second order accurate upwind differencing scheme and the results compared to available experimental data. The aim of the study was to provide a good basis for future modelling of ducted tip hydrofoils and a ducted tip propeller.

Key results from this study include the following:

1. Grid convergence studies have shown that an increase in number of cells is unlikely to cause a great difference in the pressure distribution along the hydrofoil away from the tip but will likely increase suction peaks significantly close to the hydrofoil tip.

2. Comparison with the experimental results of McAlister and Takahashi shows that more than 0.2 spanwidths away from the tip, sectional lift is predicted within 2% of the experimental data whereas closer to the tip the difference reaches up to 12%. The total lift is in good agreement with lifting line theory. The discrepancy in pressure distribution close to the tip can likely be attributed to poor grid resolution, diffusion in the turbulence model and a low order differencing scheme.

3. Comparison with the experimental results of Dacles-Mariani et al. shows good prediction of the spanwise location of the vortex core and indicates that the vortex induced pressure peak is captured reasonably well.

Future work will include developing a Pro Engineer model of a hydrofoil with a ducted tip and running simulations for the flow around it. Particular interest in future simulations is the overall performance of the hydrofoil, which is largely indicated by the overall lift coefficients, that have been shown here to be well predicted. A final stage of the research will involve simulation and optimization of ducted tip propellers.

## **CHAPTER 3 - COMPUTATIONAL STUDY OF THE FLOW AROUND A DUCTED TIP HYDROFOIL**

This chapter has been submitted as a paper to the 2002 Joint US ASME-European Fluids Engineering Summer Conference. The bibliographic reference for this paper is:

Ingvarsdottir, H., Ollivier-Gooch, C., and Green, S. I., 2002, "Computational Study of the Flow Around a Ducted Tip Hydrofoil," 2002 Joint US ASME-European Fluids Engineering Summer Conference, Montreal, Canada.

### **3.1 Abstract**

Steady flow over rounded and ducted tip hydrofoils has been studied computationally using the CFDRC-ACE(U) flow solver and a  $k-\epsilon$  turbulence model. The flow domains were gridded with a combination of C-H, H-H, tetrahedral and prism grid blocks and mesh sizes ranged from 350,000 - 550,000 cells. A good agreement in flow pattern was achieved between the numerical solutions and available experimental data. The computations show that the ducted tip hydrofoil sheds less bound circulation over the majority of the wing span than does a rounded tip hydrofoil with the same cross section and aspect ratio. Observation of the streamwise component of vorticity immediately downstream of the different hydrofoils shows that the vorticity from the ducted tip hydrofoil is shed in the shape of a duct instead of the concentrated circular vortex shed by the rounded tip hydrofoil.

### **3.2 Introduction**

All lifting surfaces that terminate in a moving fluid create tip vortices as a by-product. Tip vortices are of great importance because of their effect in several applications, such as landing separation distances for aircraft, blade/vortex interactions on helicopter blades, and propeller cavitation on ships. Tip vortices on marine propellers have two undesirable effects: they reduce the

efficiency of the blade and they may cause tip vortex cavitation. Tip vortex cavitation can cause pitting and erosion of the propeller and surrounding equipment and is also a source of vibration and noise.

Several devices and methods have been studied to reduce the effects of tip vortices on propellers. The most commonly used device is the Kort Nozzle. The Kort nozzle consists of a duct that is fitted with a small clearance around the propeller. It can improve the efficiency of highly loaded propellers up to 10% but the added wetted surface creates extra drag when less heavily loaded. Other devices or methods that have been proposed include bulbous tips on propeller blades (Crump, 1948), porous blade tips (Mani et al. 1988), small bladelets (Itoh et al., 1987) and injecting a dilute polymer solution from an orifice at the tip of a hydrofoil (Fruman and Aflalo, 1989, Chahine et al., 1993).

A number of computational studies have been done on tip vortices, both in aerodynamic and marine applications. The focus, however, has primarily been on validating methods for prediction and advancing the understanding of tip-vortex formation in general, rather than showing effects of tip modifications on tip vortices. Studies of the most relevance to the current work include computational studies by Dacles-Mariani et al. (1995) and Hsiao and Pauley (1998, 1999). Dacles-Mariani et al. carried out interactively a computational and experimental study of the wingtip vortex in the near field using a full Navier-Stokes simulation, accompanied with the Baldwin-Barth turbulence model. Although they showed improvement over numerical results obtained by previous researchers, the tip vortex strength was under predicted. Hsiao and Pauley (1998) studied the steady-state tip vortex flow over a finite-span hydrofoil, also using the Baldwin-Barth turbulence model. They were able to achieve good agreement in pressure distribution and oil flow pattern with experimental data and accurately predict vertical and axial velocities of the tip vortex core

within the near-field region. Far downstream, however, the computed flow field was overly diffused within the tip vortex core. Hsiao and Pauley (1999) also carried out a computational study of the tip vortex flow generated by a marine propeller. The general characteristics of the flow were well predicted but the vortex core was again overly diffused.

The particular wing geometry of interest in this study is one with a ducted tip. A ducted tip geometry on a hydrofoil or propeller is one in which flow-through ducts, aligned approximately with the hydrofoil/blade chord, are affixed at the hydrofoil/blade tips. The ducted tip geometry for a hydrofoil was first proposed by Green et. al (1988). Water and wind tunnel tests have shown that the flow-through ducts suppress the tip vortex roll-up, thus resulting in a substantial delay in the onset of tip vortex cavitation (Green and Duan, 1995). This comes with little change in the lift to drag ratio. The ducted tip has also been studied on a propeller. Sea trials on a ducted tip propeller and a conventional one conducted by Hordnes and Green (1998) showed that the cavitation inception index could be reduced by approximately 50% by installing the ducted tips. This came without efficiency loss. The efficiency of the ducted tip propeller is in fact up to 6% higher than the efficiency of the conventional propeller.

In the present study, steady flow over rounded and ducted tip hydrofoils has been studied computationally using the CFD-ACE(U) flow solver and a  $k-\epsilon$  turbulence model. The aim of the study was to expand our knowledge and understanding of the flow around a duct attached to the tip of a hydrofoil and thus provide a good basis for computational optimization of a ducted tip propeller blade. Numerical implementation, including a detailed description of the grid generation, is described first. This is followed by the results which contain a grid dependence study, a comparison with experimental results and a discussion. Conclusions are outlined at the end.

### 3.3 Numerical implementation

The current study considers a uniform flow past two hydrofoils with a modified 64-309 cross section. One of the hydrofoils has a rounded tip whereas the other one has a duct attached to its tip as described below. The hydrofoils, their computational domains, and the flow properties of the surrounding fluid were chosen with comparison to the experimental data of Green (1988) in mind.

#### 3.3.1 Geometry

Both hydrofoils are without twist and taper and have an aspect ratio of 1.17. The aspect ratio is based on the semi-span ( $s$ ).

The semispan of the rounded tip hydrofoil is measured from the root of the hydrofoil to the spanwise station where the rounding of the tip starts. The rounded tip is formed by creating a number of semi-circles placed at regular intervals along the chord ( $c$ ) between the upper and lower surface of the foil. The diameter of each semi-circle is approximately equal to the vertical distance between the upper and lower surface at the corresponding chordwise station. The surface is then formed by creating four sided surfaces between adjacent semi-circles.

The semi-span of the ducted tip hydrofoil is based on the average spanwise distance between the root of the foil and the intersection curve between the duct and the hydrofoil (the change in span chordwise is less than  $\pm 0.5\%$ ). The duct has an outside diameter of  $0.19c$  and is  $0.67c$  long and is attached flush with the hydrofoil trailing edge, with its central axis aligned with the camberline. The duct has thus a slight curvature to it. The thickness of the wall is  $0.013c$  at the front top and bottom of the duct, but tapers off to almost no thickness along the whole outboard side of the duct as well as towards the trailing edge of the duct. The shape of the duct and its attachment to the foil have been made to resemble as closely as possible the original ducted tip hydrofoil for

which the experimental results are available. It is however impossible to replicate the original hydrofoil perfectly; the greatest difference between the two occurs in the area where the duct and the hydrofoil meet. On the original hydrofoil a fillet was added to smooth the intersection but that fillet has not been replicated in the computational model due to the difficulty in creating and meshing a hydrofoil with such a fillet.

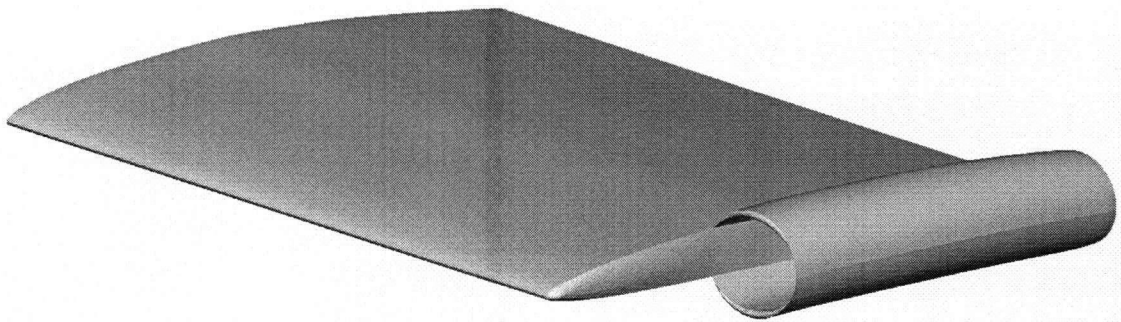


**Figure 3.1** The ducted tip hydrofoil.

The dimensions of the computational domain were chosen so that the cross section perpendicular to the freestream flow would be the same as the corresponding cross section of the tunnel in which the experiments were performed. The flow domain is 2 chord lengths high and wide. The domain extends 2 chord lengths downstream of the trailing edge and 1.25 chord lengths upstream of the leading edge of the hydrofoil. The hydrofoils are tilted around the quarter chord line when run at an angle.

### **3.3.2** *Grid Generation*

Several grid generation methods have been explored in attempts to resolve the flow near the tip vortex core and the hydrofoil surface. The multi-block grids that were used for this study con-

sist of structured hexahedral, semi-structured prismatic, and unstructured tetrahedral blocks. The grids were generated with CFD-GEOM from CFD Research Corporation and their basic structure will be described below.

**Gridding the Rounded Tip Hydrofoil.** A C-mesh is wrapped around a two dimensional section of the hydrofoil and extruded along the foil from the symmetry plane to the opposite side of the domain to form a C-H mesh (Figure 3.2). The cavity formed between the tip of the foil and the opposite wall is filled with an H-H mesh extending approximately from 3% of the chord length to 95% of the chord length of the hydrofoil. The leading and trailing edge parts of the tip are gridded with a triangular surface grid, which is then extruded across the domain (z-direction) to form a prismatic grid that matches the C-H and H-H blocks (Figure 3.3). These regions were meshed prismatically to avoid very skewed cells at the leading edge and high aspect ratio cells at the trailing edge tip.

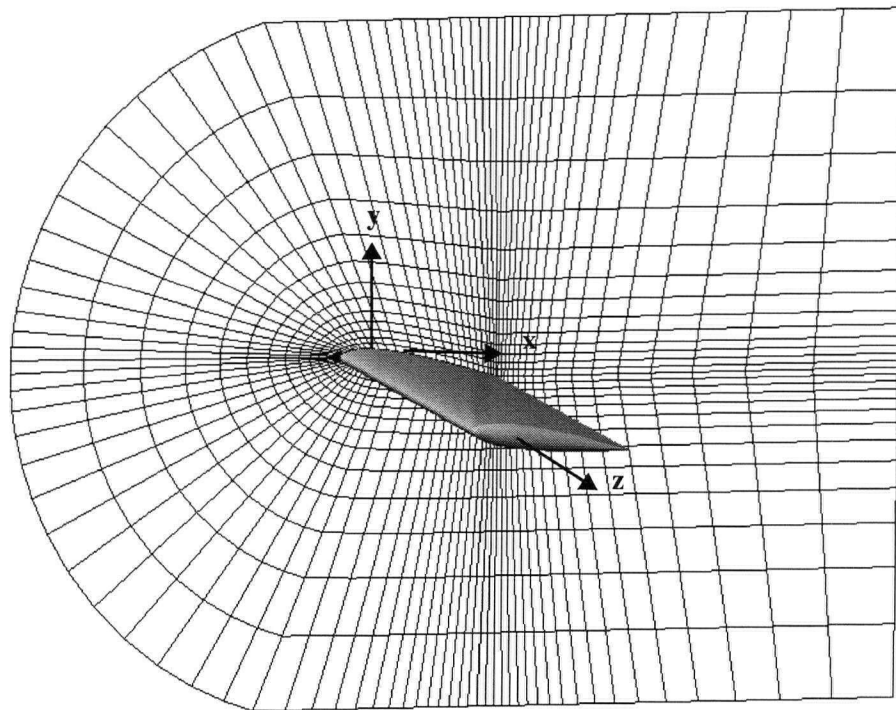
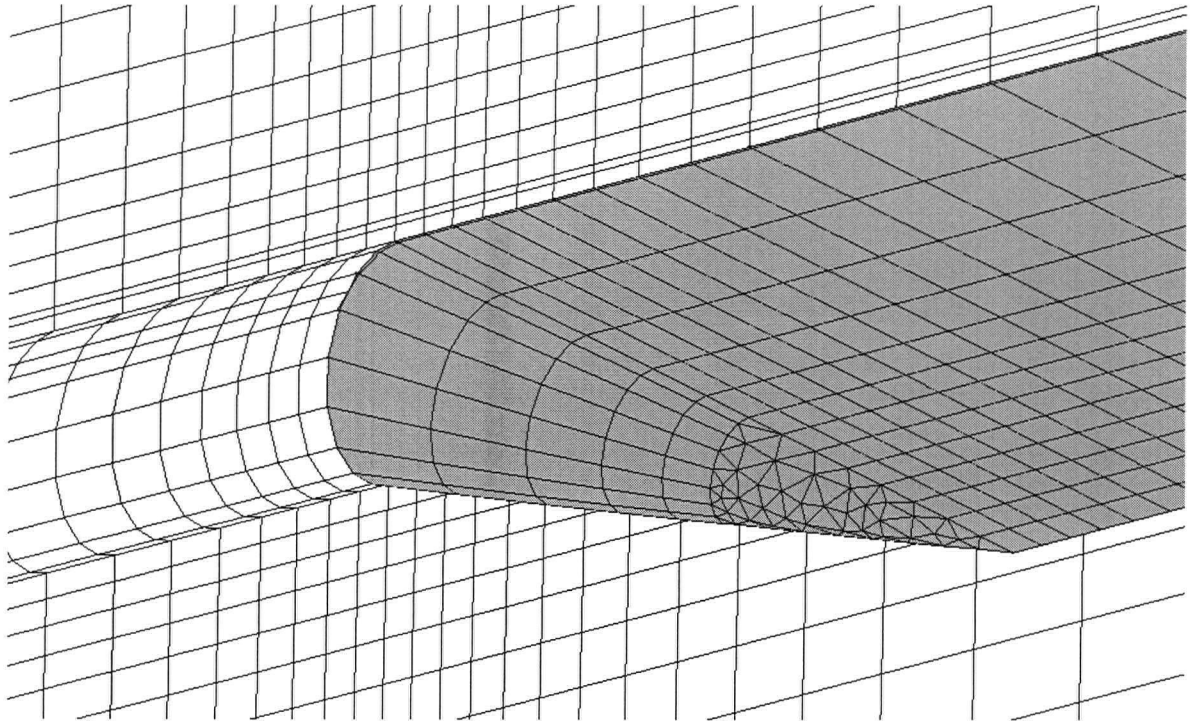


Figure 3.2 The 2D C-mesh is extruded along the foil in the z-direction to the plane opposite to the tip of the hydrofoil.



**Figure 3.3** An example of a coarse surface mesh on the tip at the trailing edge of the hydrofoil and a cut of the grid in the x-z plane.

**Gridding the Ducted Tip Hydrofoil.** The duct introduces greater meshing challenges than the rounded tip. The aim of the gridding scheme used was to mesh the region right in front of the duct and inside it in a fashion that allows the rest of the domain to be gridded with one prismatic block and C-H and H-H blocks, as for the rounded tip hydrofoil. This was done in the following way.

The front opening of the duct is gridded with an H-grid in the center of the duct and another H-grid running around the central H-grid along the duct wall, as seen in Figure 3.4. This allows good control of the cell distribution. These two H meshes are extruded through the duct and all the way to the outlet boundary of the flow domain. The front face is also gridded with a triangular mesh and an arbitrary interface is thus created at this face, as can be seen in Figure 3.5. The tip of the foil in front of the duct as well as the front faces of the duct are gridded with triangular surface

grids. A “capsule” with triangular surface grids is made and used to create a tetrahedral block (Figures 3.5 and 3.6). The upper and lower surfaces of the “capsule” are now also gridded with a structured grid that matches the surface grid of the hydrofoil (Figure 3.7). The remainder of the gridding is done in basically the same way as the gridding of the rounded tip foil. A C mesh is extruded from the root wall along the surface, over the top of the duct and then straight across the flow domain to the opposite tunnel wall. The gap formed is filled with a prism mesh, which is formed by an extrusion of the triangular surface grid on the “capsule”, and an H-H mesh, which is formed by an extrusion of an H-grid that is on the outboard side of the duct and the circular block that extends from the outlet of the duct to the end of the flow domain (Figure 3.8)

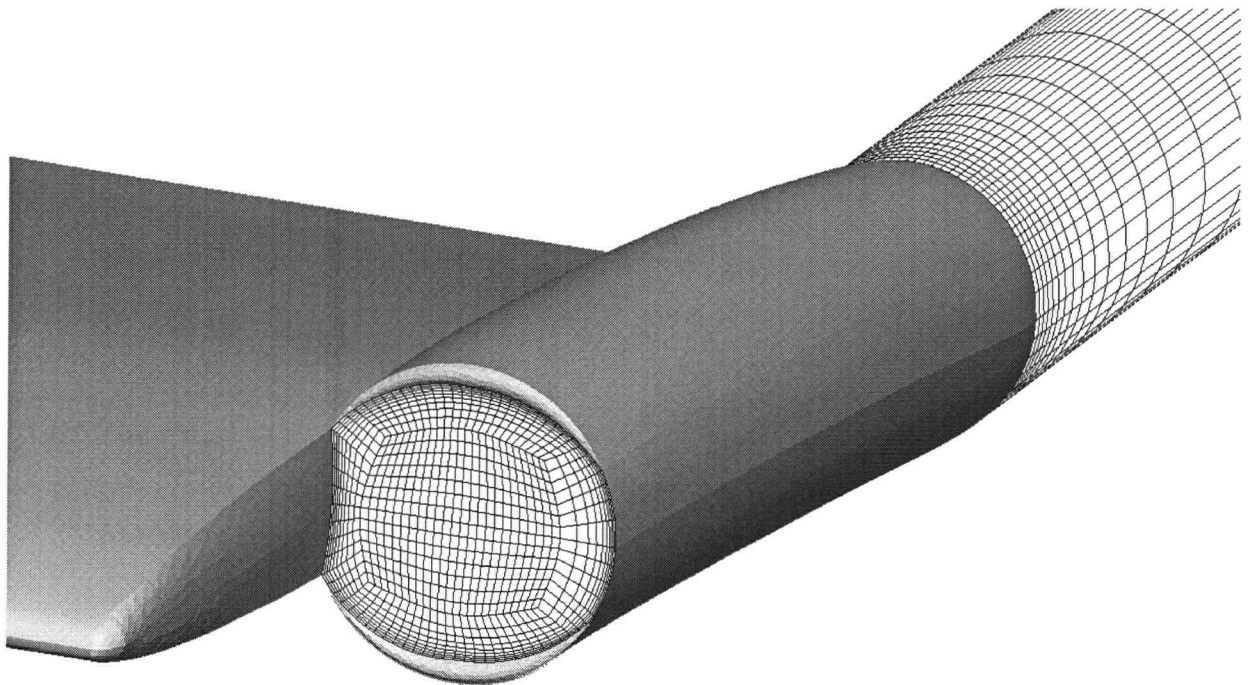


**Figure 3.4** Blocks consisting of H-H meshes run through the duct and continue in the streamwise direction to the end of the flow domain.

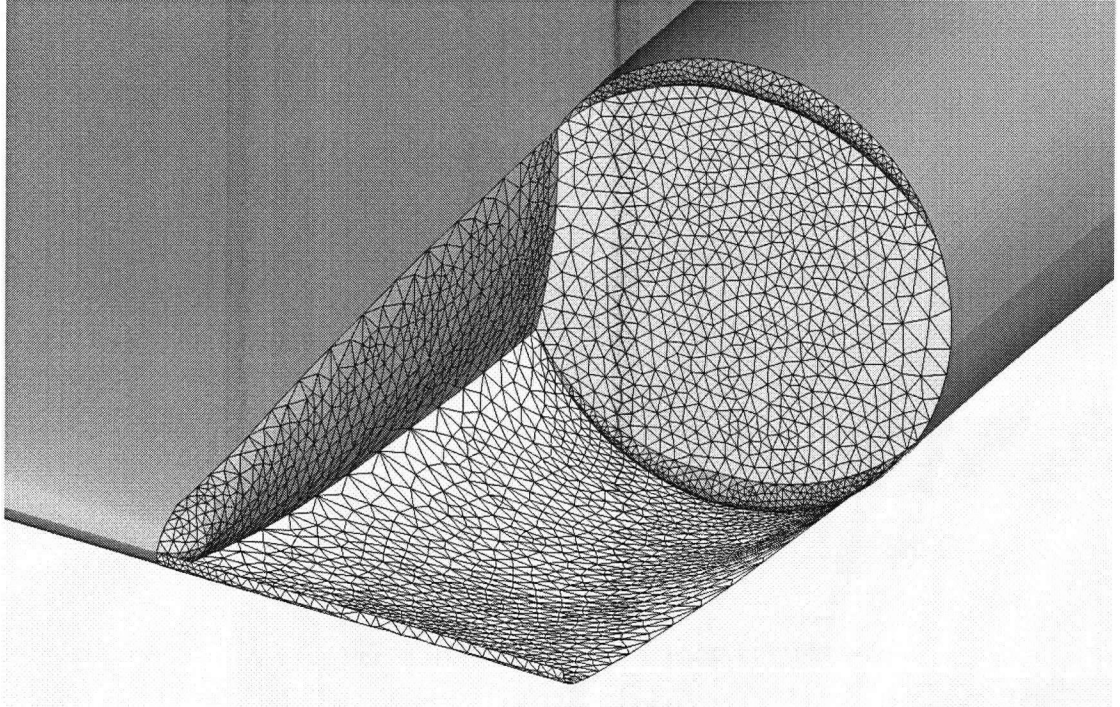


**Figure 3.5** Triangular gridding on hydrofoil tip and front of duct and formation of tetrahedral “capsule”.

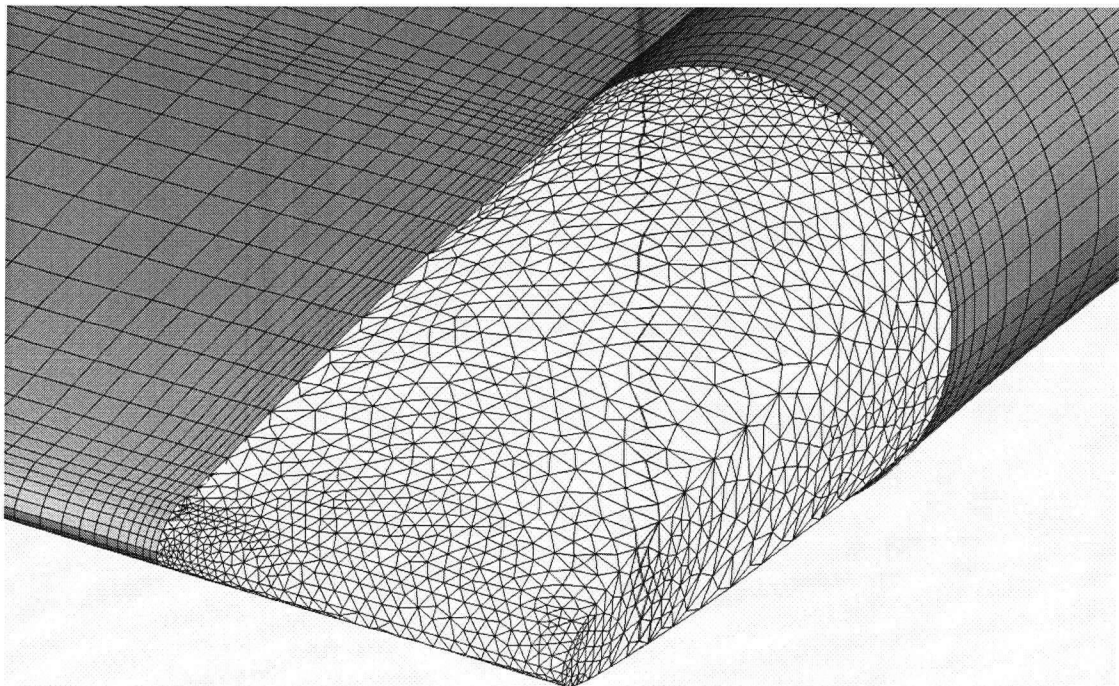


**Figure 3.6** Tetrahedral gridding in front of the duct.

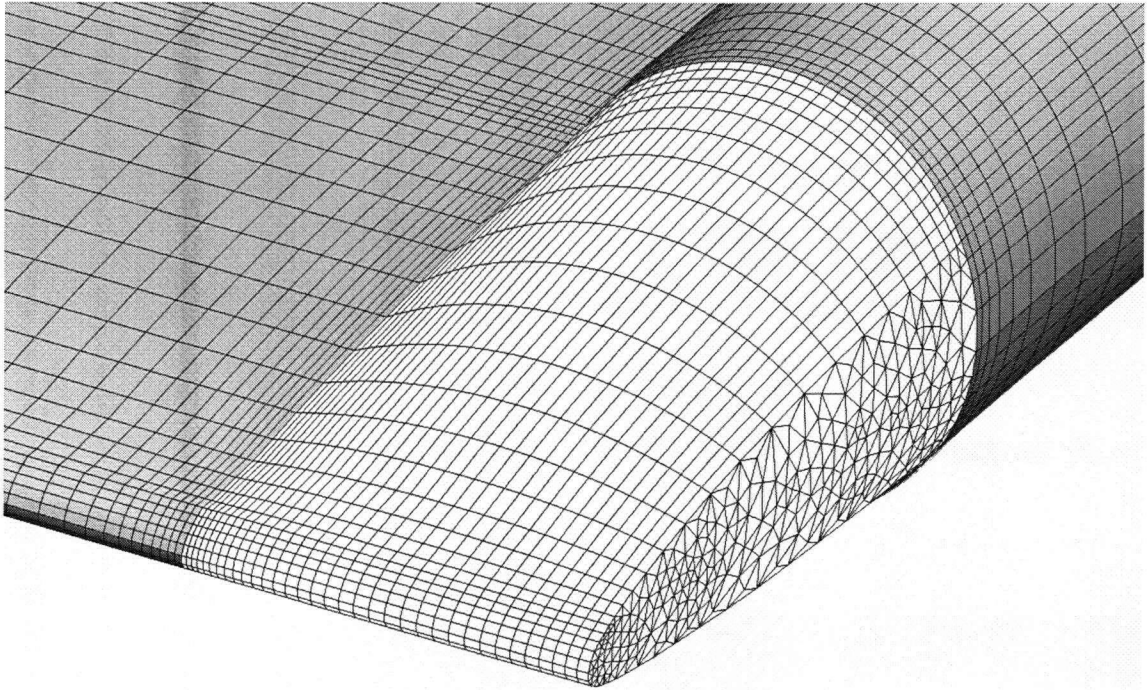


**Figure 3.7** The top and bottom sides of the “capsule” are also gridded with an H grid which matches up with the surface grid on the hydrofoil.

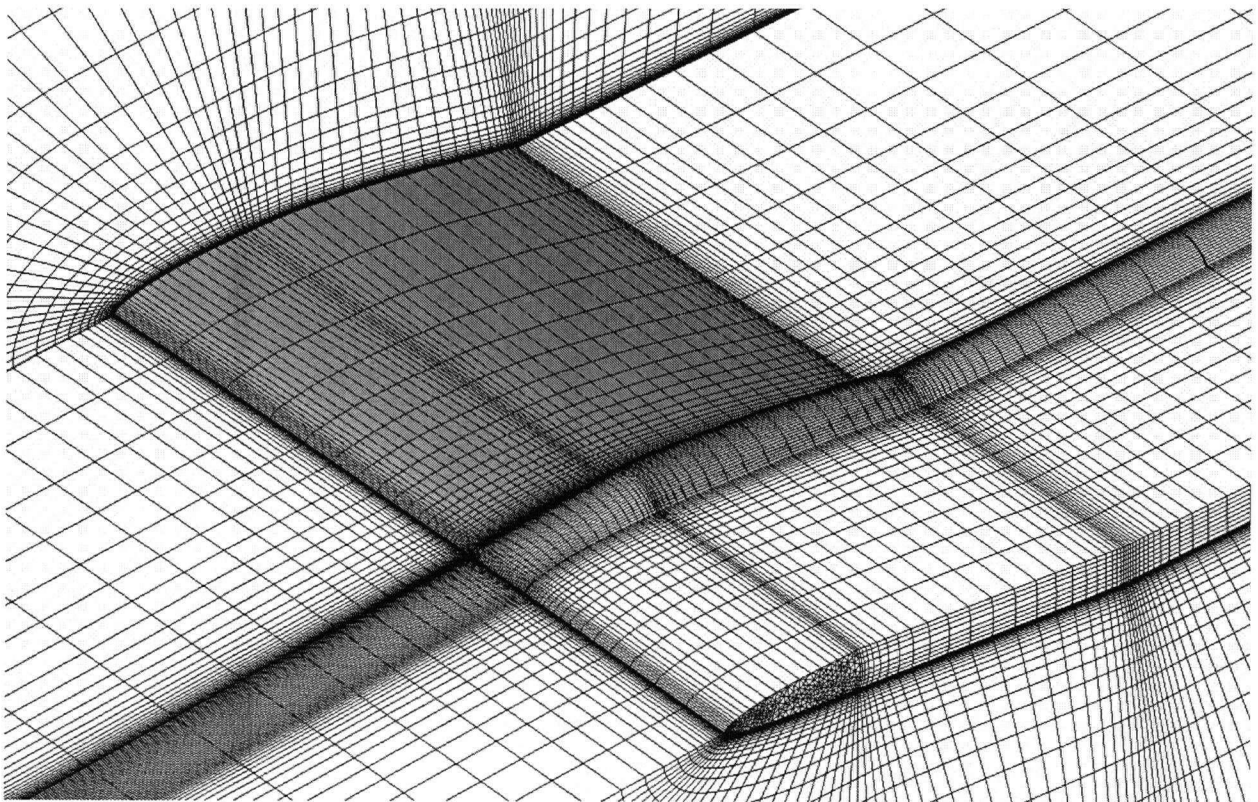


**Figure 3.8** Grid topology for the ducted tip hydrofoil.

### **3.3.3 Numerical Method**

The pressure-based, finite-volume flow solver CFD-ACE(U) from CFDRC was used in this study. The code uses unstructured/hybrid grids to integrate the Navier-Stokes equations. Cases were run with a k- $\epsilon$  turbulence model and a second-order accurate upwind differencing scheme.

### **3.3.4 Boundary Conditions**

Since each grid consists of multiple blocks, as described above, there are two types of boundaries where conditions have to be specified: 1) the physical boundaries such as inflow, outflow and walls; and 2) the block-interface boundaries across which all flow quantities must be continuous.

For the physical boundaries the freestream velocity was specified for the inlet and constant pressure was specified for the outlet. A no-slip flow condition was used for the solid hydrofoil surface. Boundaries corresponding to the walls of the tunnel were specified as slip walls.

## **3.4 Results**

The ducted and rounded tip hydrofoils were studied at angles of attack  $\alpha = 7^\circ$  and  $\alpha = 12^\circ$  and a Reynolds number  $Re = 1.2 \times 10^6$ . Before performing these computations and comparing the results with the available experimental data, a grid convergence study was carried out for the rounded tip hydrofoil to assess the influence of grid density. The grid dependence study will be described below followed by a comparison with experimental results and discussion.

### **3.4.1 Grid Dependence**

The primary grid used for the rounded tip hydrofoil in this study has a total of approximately 536,000 cells. The C-H grid has 209x34x73 grid points in the streamwise, surface normal and spanwise directions, respectively. 151 of the 209 streamwise grid points and 44 of the 73 span-

wise grid points are used on the hydrofoil. The first grid spacing on the hydrofoil surface is specified at 0.0006 chord length above the hydrofoil surface. The H-H grid extending from the midsection of the tip has 54x15x30 grid points and the nose and tail prism grids have 4872 and 15428 cells respectively.

Prior to making the primary grid, grids with fewer cells and/or a different grid distribution were made and tested. The cases run are labelled as Grid 1, 2, 3 and 4 with Grid 4 being the grid described above. The main difference in Grids 1, 2 and 3 from Grid 4 is as follows: The first grid has approximately 340,000 cells with the first cell spacing above the hydrofoil surface 0.0012 chord length high. The second grid has approximately 475,000 cells with a higher local density near the hydrofoil tip and tip-vortex core but otherwise the same distribution as Grid 1. The third grid has the same number of cells as the primary grid (Grid 4) but a larger first cell spacing on the tip of the hydrofoil.

The flow angles, quantified by measuring the angles at the trailing edge on the pressure and suction surfaces, and along the tip of the hydrofoils, obtained from the different density grids, are shown in Figures 3.9, 3.10 and 3.11 (refer to Figure 3.12 (a) and (b) for the definitions of  $\phi$  and  $\epsilon$ ). As may be seen, there is negligible difference between the results from Grids 3 and 4 for the suction and pressure side of the hydrofoil. The flow angles on the side of the foil, which are referred to in Figure 3.11 as downwash angles, are the surface flow angles made by the experimental smear lines/computed flow vectors with respect to the chordline, measured/computed on the chordline at the tip. These angles increase more along the chordline with each grid and are clearly not grid converged, although they do approach towards the experimental solution. It is clear that the first cell spacing on the tip has a significant effect on the flow angles. Further grid refinement, however, resulted in divergence of the computations which can be attributed to too small  $y^+$  val-

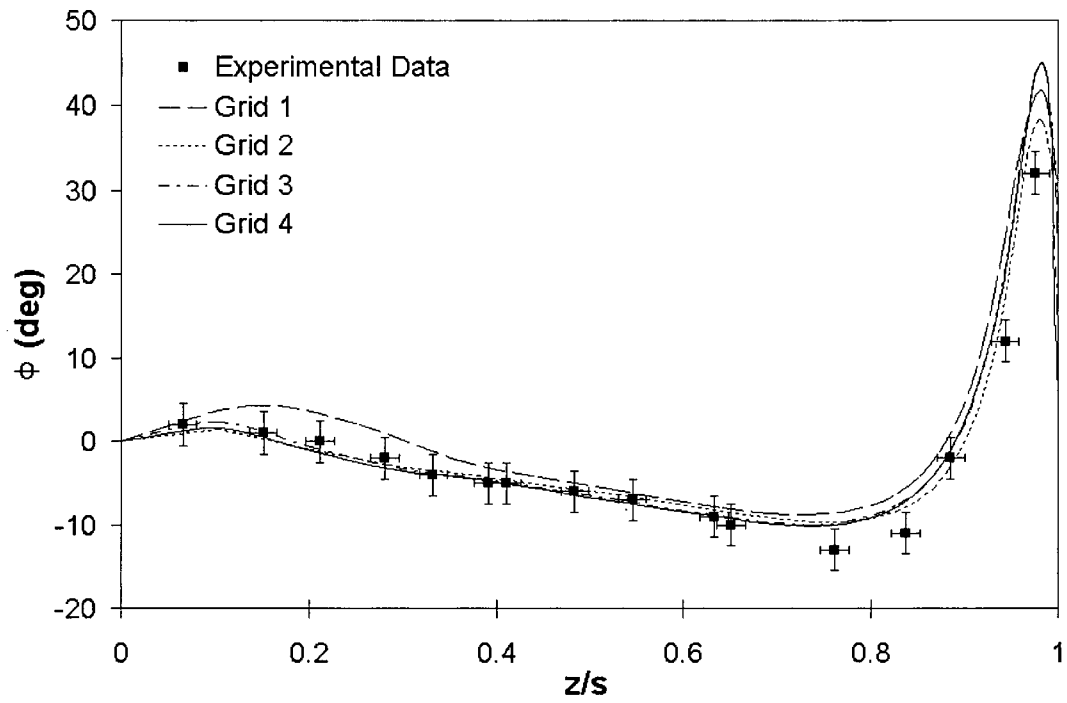


Figure 3.9 Comparison of inboard flow angles at trailing edge, suction side at  $\alpha = 7^\circ$ . Refer to Figure 3.12 (a) for the definition of  $\phi$ .

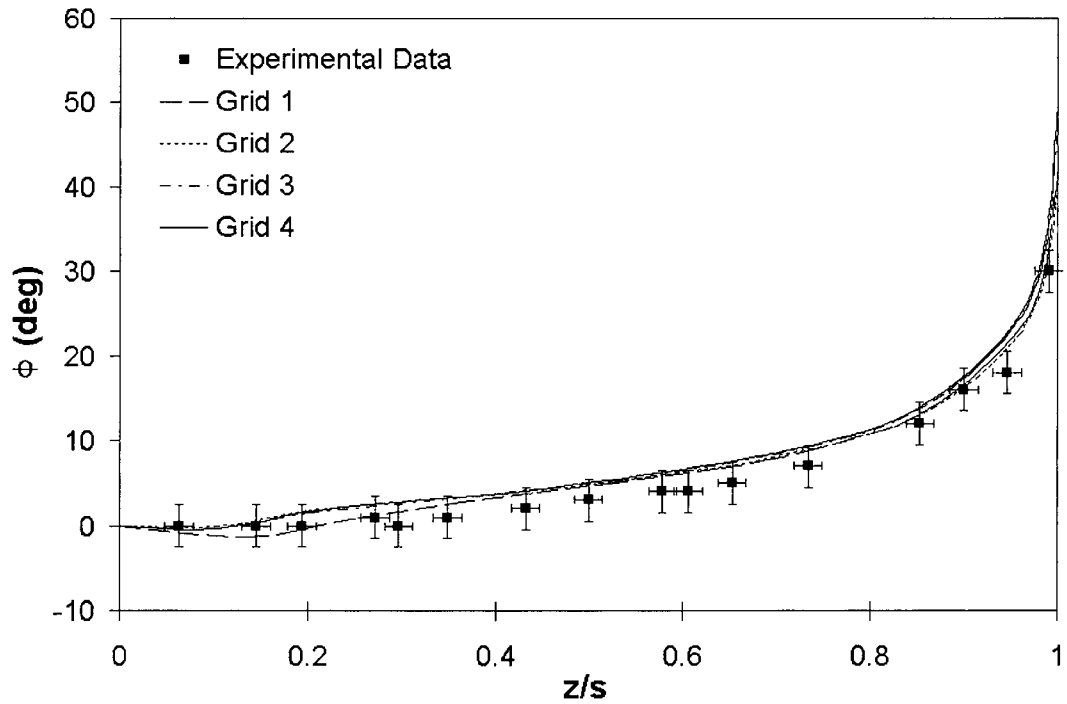
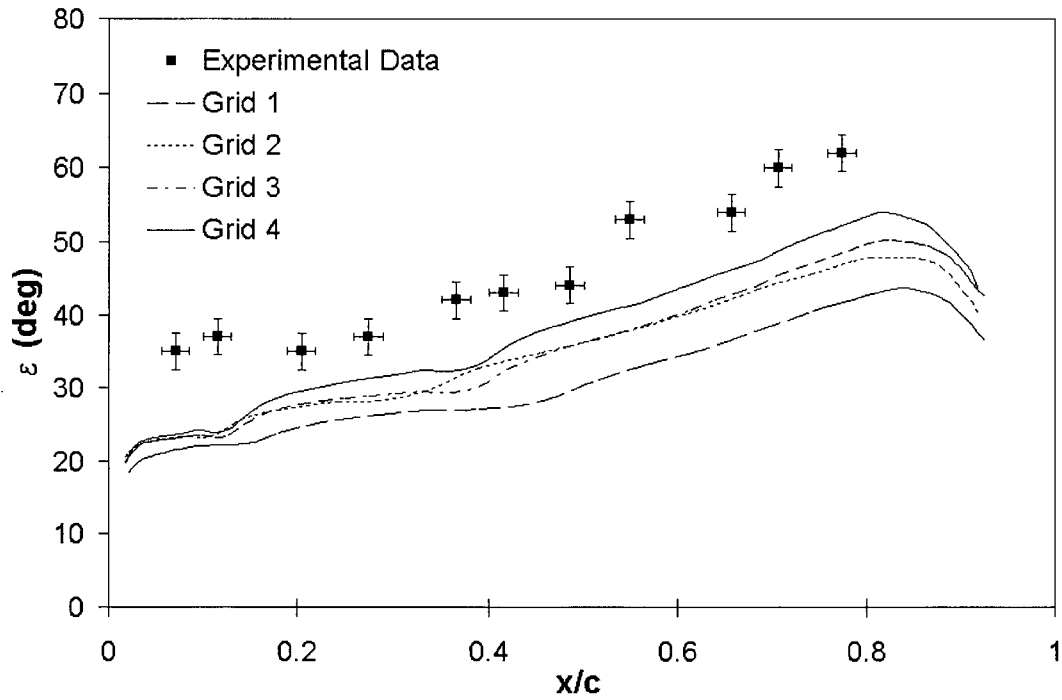


Figure 3.10 Comparison of inboard flow angles at trailing edge, pressure side at  $\alpha = 7^\circ$ .



**Figure 3.11 Comparison of downwash flow angles at the tip at  $\alpha = 7^\circ$ . Refer to Figure 3.12 (b) for the definition of  $\epsilon$ .**

ues (below  $y^+ = 11.5$ ) near the wall in some regions. The  $k-\epsilon$  turbulence model is not a near wall model and causes divergence problems once the  $y^+$  values in the first cell get this low.

The lift coefficient was computed for the 4 cases. The difference between the lift coefficients computed from grids 2, 3 and 4 was less than 1% (Table 3.1)

**Table 3.1 Comparison of Lift Coefficients ( $C_L$ ).**

	Grid 1	Grid 2	Grid 3	Grid 4
$C_L$	0.528	0.546	0.545	0.543
% Difference from Grid 4	-2.8%	-0.6%	-0.4%	

### 3.4.2 Comparison with Experimental Results

The primary comparison that is done here is one of surface velocity vectors obtained from the computations, and surface flow visualization (SFV) photographs from experiments done by

Green (1988). The grids used for the computations for the rounded tip hydrofoil have the same structure and cell distribution as the primary grid (Grid 4) described above. The grids for the ducted tip hydrofoils have a total of approximately 402,000 cells, of which around 64,000 cells are tetrahedral cells that lie within the “capsule” block previously described, and 8700 are prismatic cells in the block that extends from the side of the “capsule” to the plane opposite to the root wall. The remaining blocks are structured and will not be described in detail here. The first cell above the hydrofoil surface, and the exterior and the interior of the duct, generally extends 0.001c into the flow domain.

Surface vector pictures for the cases run at  $12^\circ$  angle of attack are displayed next to the corresponding SFV photographs in Figures 3.12 and 3.13. As may be seen the agreement between computations and experiments is overall very good for the *rounded tip* hydrofoil at  $\alpha = 12^\circ$ . Very good agreement was seen between surface vector plots and SFV photographs at  $\alpha = 7^\circ$  as well. Some difference is observed on the suction side close to the root wall, where a significant spanwise velocity component captured in the SFV photographs is not present in the computational results. This spanwise velocity component is due to an interference vortex near the wing root (Green and Duan 1995) and is not captured in the computations at all since the root wall is modelled as a slip wall. This applies to both rounded and ducted tip hydrofoils at both angles of attack studied. Another difference, which is further quantified in Figure 3.19, is significantly lower flow angles, relative to the chordline around the tip, for the computed hydrofoil than the experimental one. This difference is especially great towards the leading edge tip. This difference is even greater for the  $7^\circ$  case as seen in Figure 3.18. The surface flow angles around the tip are very dependent on the location of the vortex initial rollup on the tip as well as the near wall behaviour of the boundary layer. It is likely that the discrepancy between the computational and experimen-

tal flow angles around the tip can be partly attributed to a poorly resolved boundary layer. The better results achieved for the rounded tip hydrofoil at  $\alpha = 12^\circ$  can be attributed to a larger tip vortex which is thus better grid resolved.

The agreement between computations and experiments for the *ducted tip* hydrofoil is also overall quite good, as may be seen in Figure 3.13. The agreement between the SFV photographs and the surface vector plots is excellent on the pressure side and very good on the duct of the hydrofoil as well. The agreement was also very good for the  $7^\circ$  case. The surface flow on the suction side is very well predicted at the front part of the hydrofoil but less so towards the trailing edge, as can be seen clearly in Figure 3.15, where the flow angles towards the tip at the trailing edge are much different from those measured from the SFV photographs. This difference was believed to be caused by a lack of a fillet between the duct and the hydrofoil in the computational model. In order to test that hypothesis, the flow angles measured from a SFV photograph of a ducted tip hydrofoil with less fillet, tested experimentally under the same flow conditions as the foils compared to here and  $\alpha = 7^\circ$ , were also compared to the computational flow angles (Figure 3.14). The hydrofoil with the smaller fillet has significantly greater (negative) values of  $\phi$  near the tip on the suction side. This observation supports the argument that the difference between experiments and computation is largely due to the absence of a fillet in the computational model. Referring to Figures 3.13 (a) and (d), separation is seen at the leading edge of the computational and experimental hydrofoils at  $\alpha = 12^\circ$ . The separation occurs towards the root of the hydrofoil and the agreement between computation and experiment is remarkably good. Separation at the leading edge on the experimental ducted tip hydrofoil starts at the root and ends at between 57% and 64.5% of the span of the hydrofoil. The same change happens at around 63% of the span of the computational ducted tip hydrofoil.

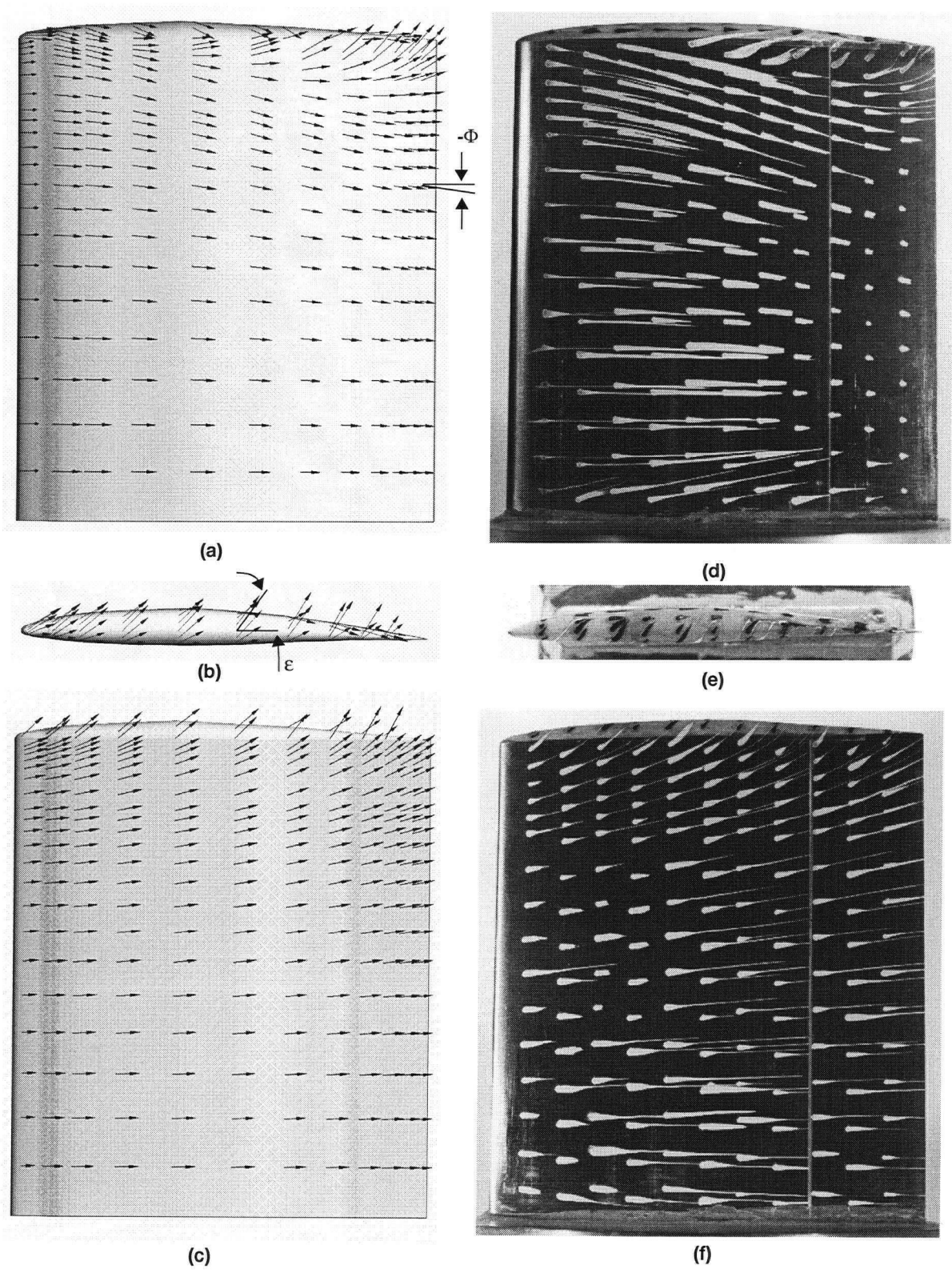
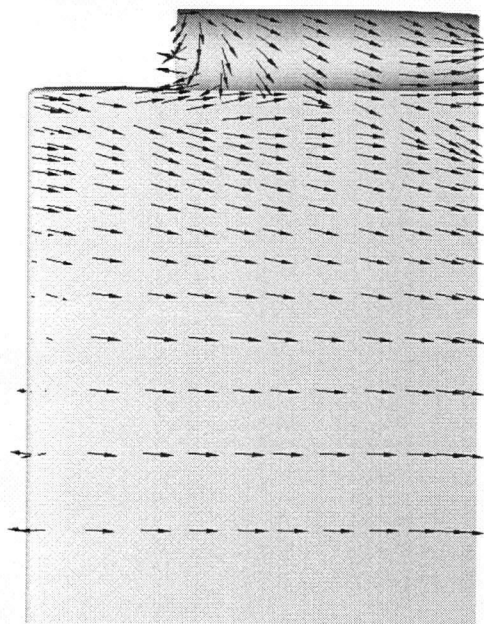
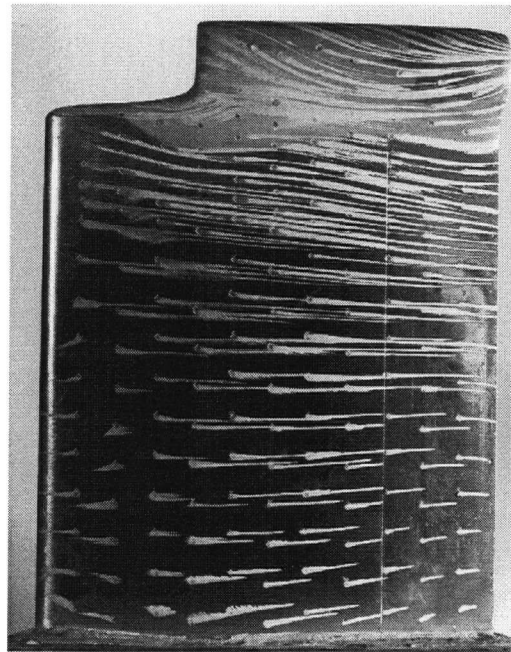


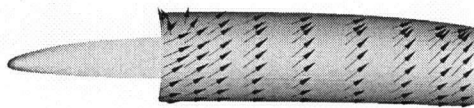
Figure 3.12 Surface vector pictures of the (a) suction side, (b) tip and (c) pressure side and SFV photographs of the (d) suction side, (e) tip and (f) pressure side of the rounded tip hydrofoil at  $\alpha = 12^\circ$ .



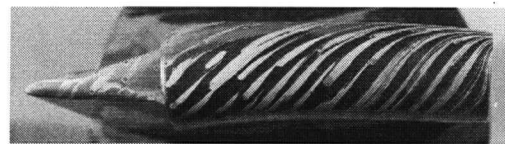
(a)



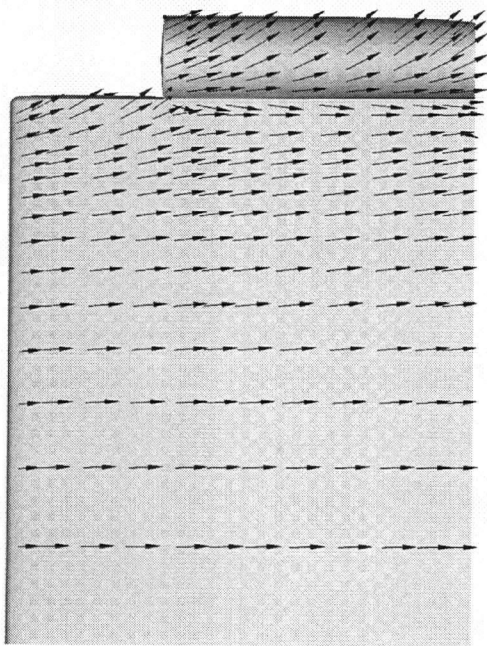
(d)



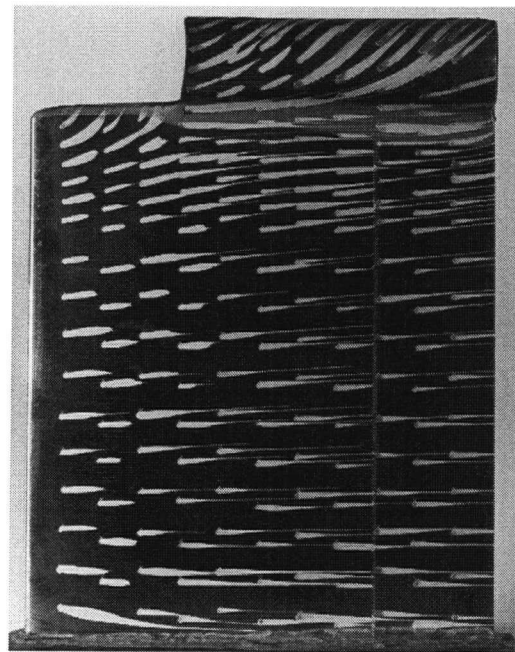
(b)



(e)



(c)



(f)

**Figure 3.13** Surface vector pictures of the (a) suction side, (b) tip and (c) pressure side and SFV photographs of the (d) suction side, (e) tip and (f) pressure side of the ducted tip hydrofoil at  $\alpha = 12^\circ$ .

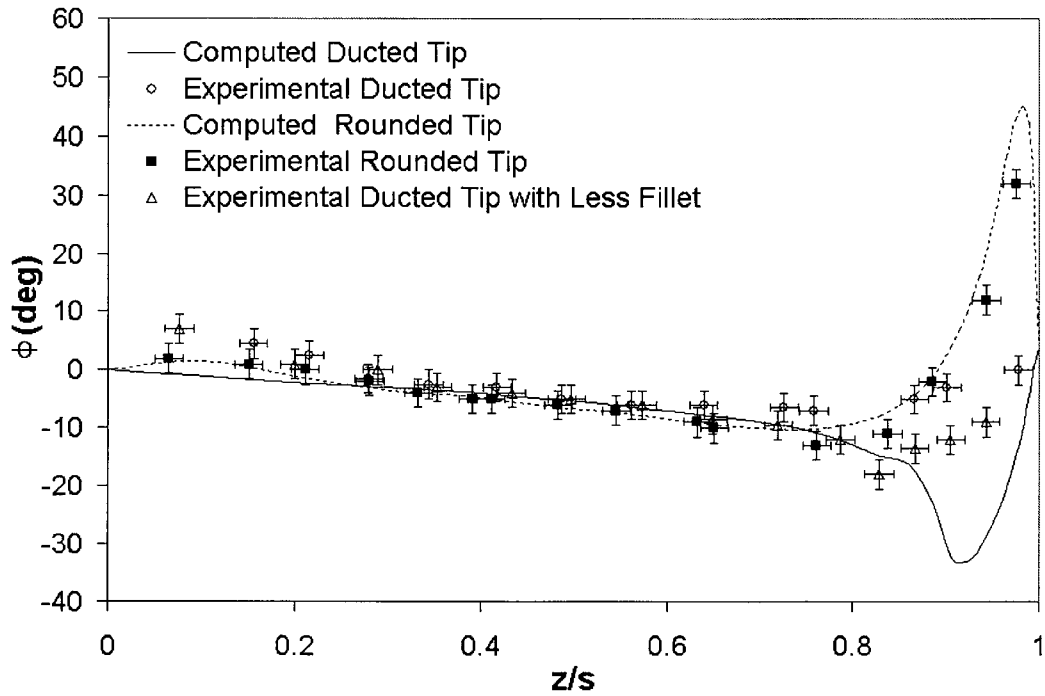


Figure 3.14 Inboard flow angles at the trailing edge on the suction side at  $\alpha = 7^\circ$ .

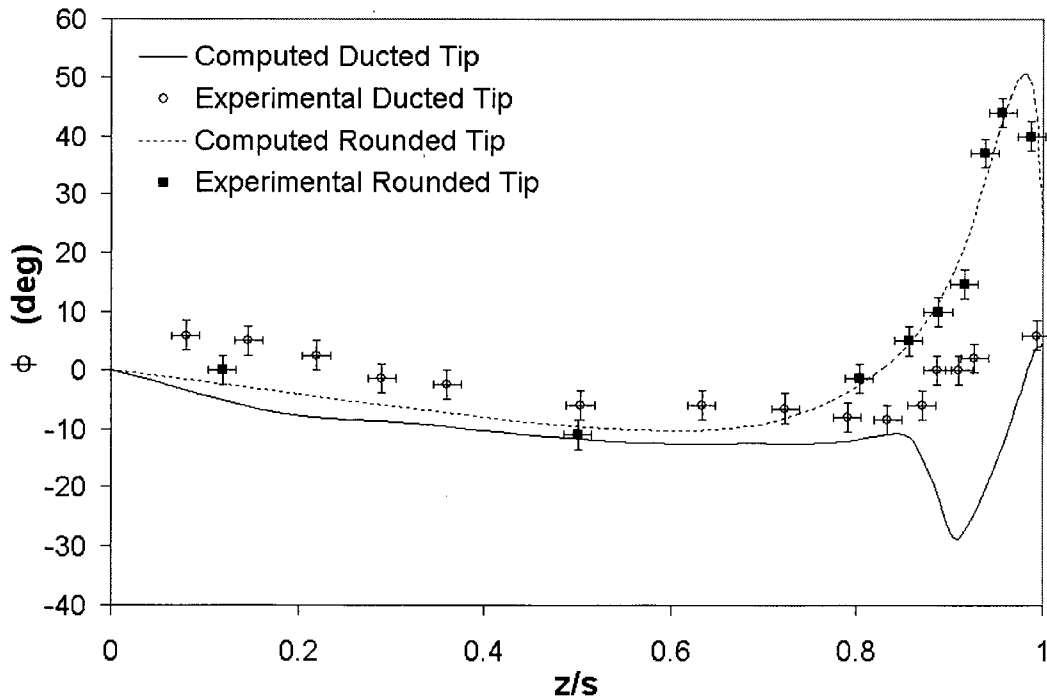


Figure 3.15 Inboard flow angles at the trailing edge on the suction side at  $\alpha = 12^\circ$ .

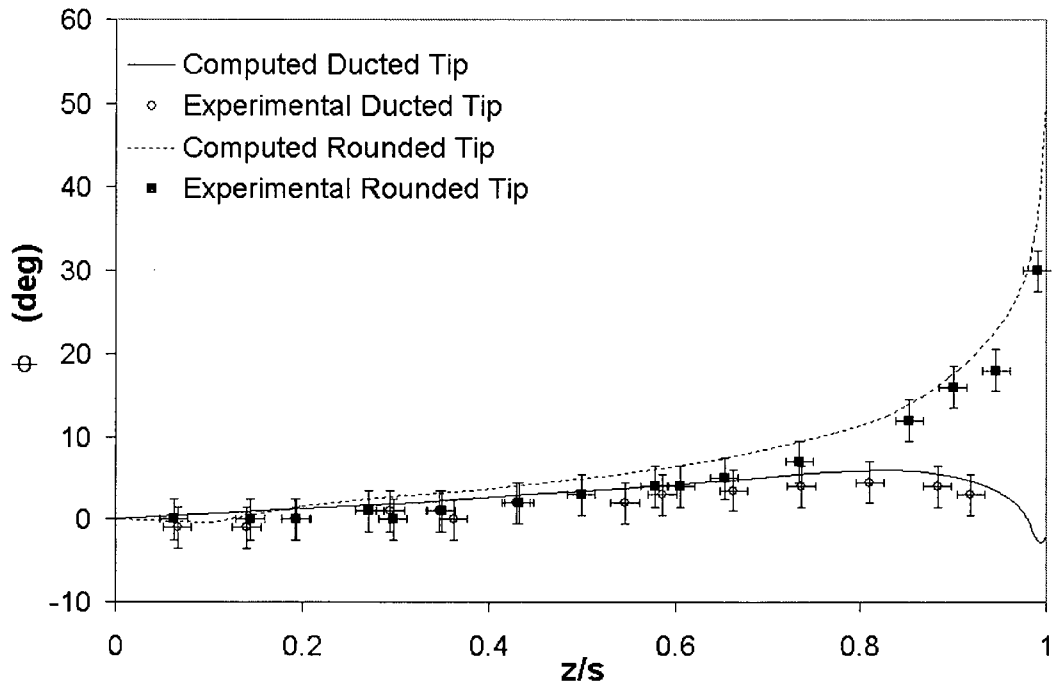


Figure 3.16 Inboard flow angles at the trailing edge on the pressure side at  $\alpha = 7^\circ$ .

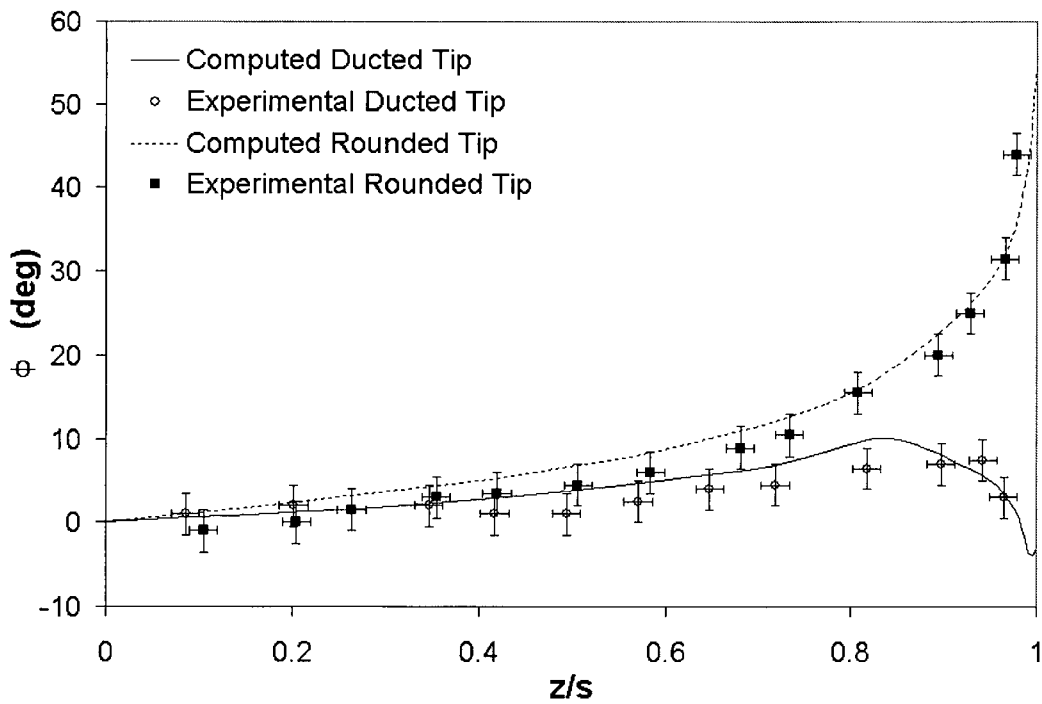


Figure 3.17 Inboard flow angles at the trailing edge on the pressure side at  $\alpha = 12^\circ$ .

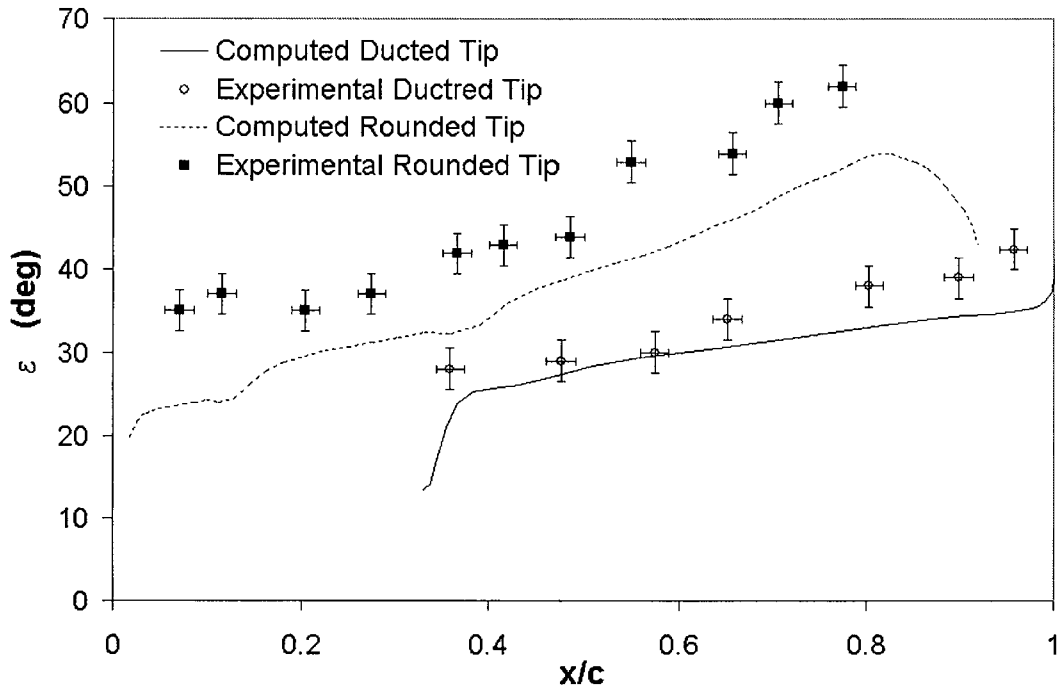


Figure 3.18 Downwash flow angles at the tip at  $\alpha = 7^\circ$ .

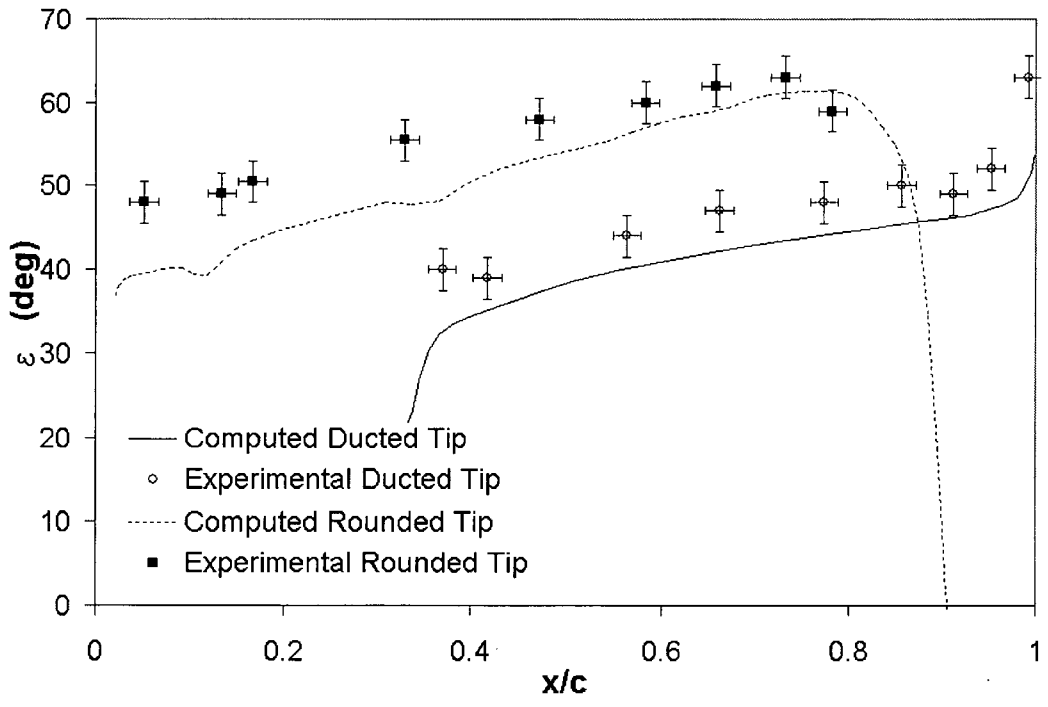
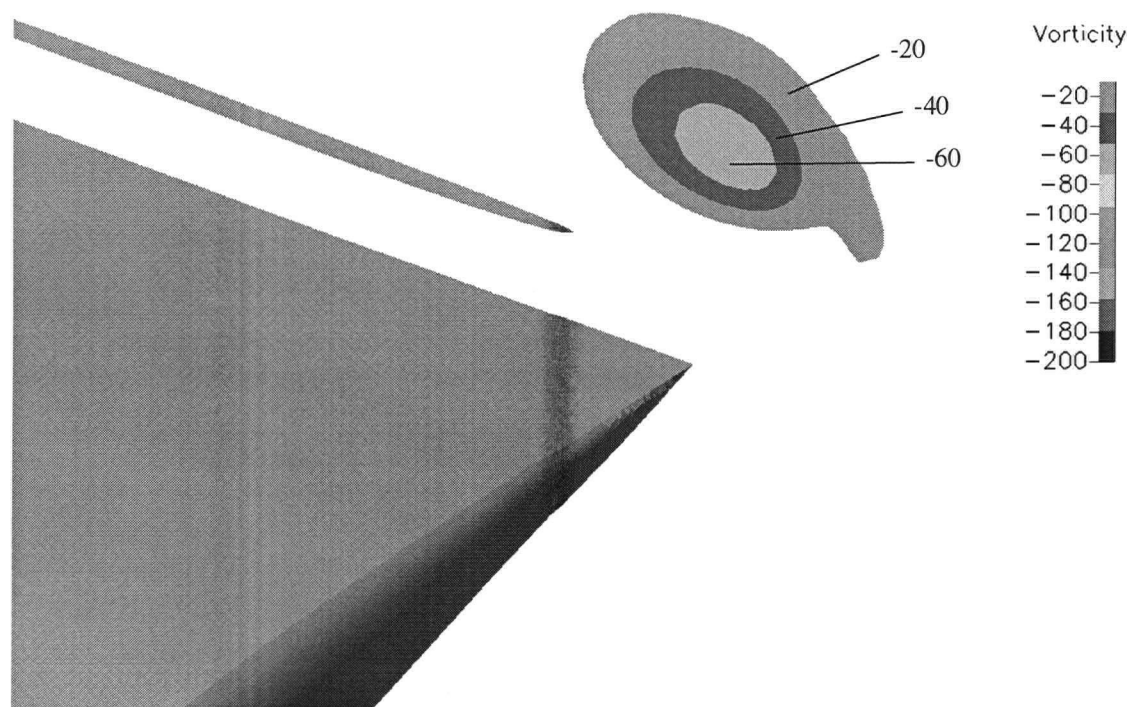


Figure 3.19 Downwash flow angles at the tip at  $\alpha = 12^\circ$ .

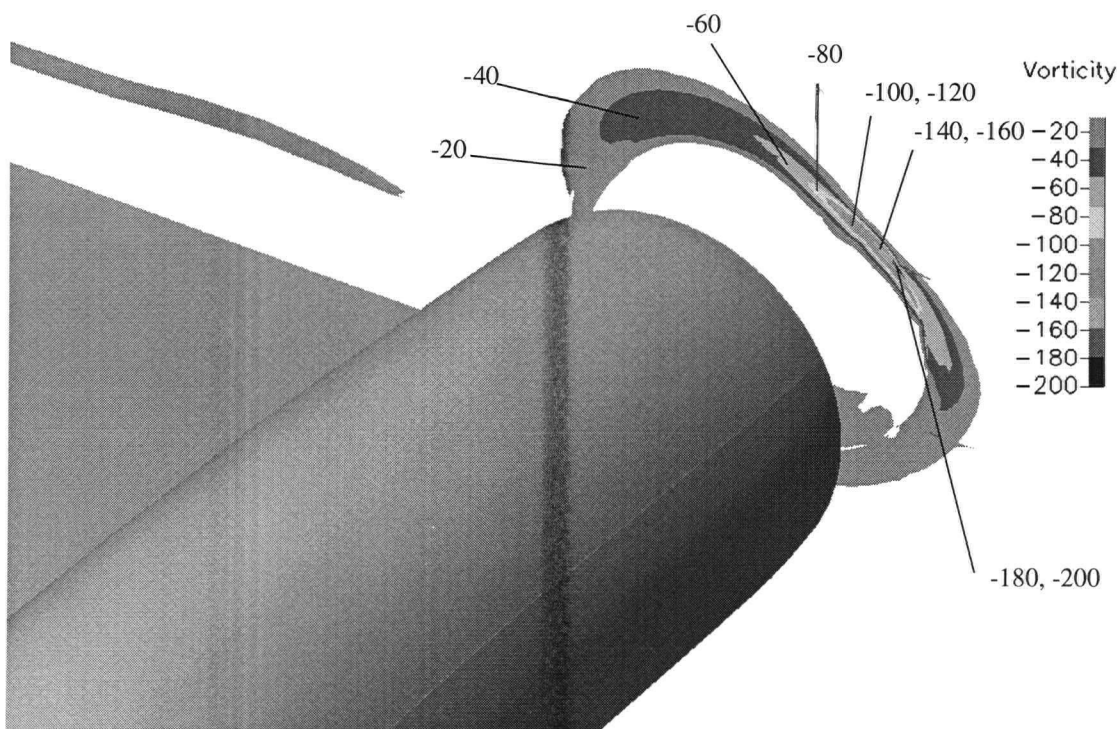
Apart from validating the computational results with experimental data through surface flow visualization on the ducted and rounded tip hydrofoils, the axial and tangential velocities of the trailing vortex were studied. Computations were performed on the rounded tip hydrofoil at  $\alpha = 10^\circ$  and  $Re = 5.2 \times 10^5$  with comparison to the experimental data of Green (1988) in mind. The computed axial velocity  $U/U_\infty$  in the vortex core immediately downstream of the hydrofoil was 1.47, which compares well to a mean axial velocity of  $U/U_\infty = 1.53 \pm 0.17$ , measured in the center of a vortex core of a rounded tip hydrofoil of similar shape (NACA 66-209 cross section) and same aspect ratio at the same operating conditions. The corresponding maximum tangential velocities were  $(U_\theta/U_\infty)_{\text{computational}} = 0.83$  and  $(U_\theta/U_\infty)_{\text{experimental}} = 0.80$ .

### 3.4.3 Discussion

Comparing the surface flow over the rounded and ducted tip hydrofoils is a good way to assess qualitatively the performance of the different geometries. It is observed from the computations in Figures 3.14 - 3.17, as was seen earlier in experiments, that the spanwise velocity component at the trailing edge pressure and suction side, despite the fillet problem, is substantially less than that of the rounded tip. The difference in spanwise velocity component suggests that the ducted tip hydrofoil sheds less circulation over the hydrofoil surface than does the rounded tip hydrofoil. The tangential velocities on the duct suggest that vorticity is shed from the duct. Computations of vorticity prove this. The x-component of streamwise vorticity immediately downstream of the trailing edge of the hydrofoils ( $x/c = 1.05$ ), in the plane normal to the freestream flow direction, was computed and is displayed in Figure 3.20. The tip vortex behind the rounded tip hydrofoil is concentrated in a circle with the highest vorticity in the centre of the circle whereas the vorticity from the ducted tip hydrofoil is shed in a ring with the same shape as the duct, with the highest vorticity located on the outboard side of the duct. Given this, it would be



(a)



(b)

Figure 3.20 The x-component of vorticity in the x-z plane right behind the trailing edge ( $x/c = 1.05$ ) of the (a) rounded tip and (b) ducted tip hydrofoil at  $\alpha = 12^\circ$  and  $Re = 1.2 \times 10^6$ .

expected that the lift along the hydrofoil surface of the ducted tip hydrofoil would be higher than the lift on the rounded tip hydrofoil. Sectional lift coefficients computed by integrating the pressure over several spanwise stations at  $\alpha = 7^\circ$  on both hydrofoils indeed support that contention. As may be seen in Figure 3.21 the ducted tip hydrofoil generates greater lift on all spanwise stations computed. Higher sectional lift coefficients of the ducted tip geometry at the root of the hydrofoil are consistent with the hypothesis that the ducted tip geometry has greater bound circulation at the root and sheds its circulation only close to the tip.

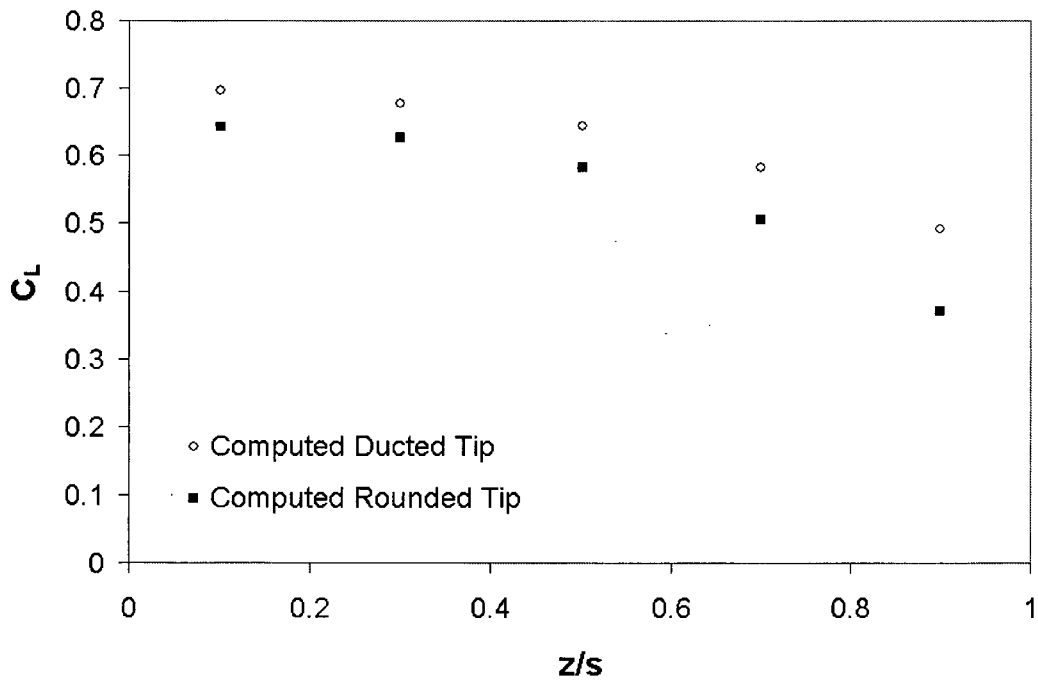


**Figure 3.21** Sectional lift along spanwise stations of the computational hydrofoils at  $\alpha = 7^\circ$  and  $Re = 1.2 \times 10^6$ .

Having established that the vorticity shed from the duct forms a circle with a much larger diameter than the rounded tip vortex, it is expected that the minimum pressure in the trailing vortex of the ducted tip hydrofoil is significantly higher than that of the rounded tip hydrofoil. This is in fact the case. The minimum computed pressure coefficients in the y-z plane at  $x/c = 1.05$  and  $\alpha$

= 12° are  $C_{p \text{ ducted tip}} = -1.07$  and  $C_{p \text{ rounded tip}} = -2.94$ . This implies that the ducted tip is likely to inhibit cavitation inception, a finding that is in agreement with observations by Green and Duan (1995). They measured cavitation inception indices at different angles of attack and found the inception index for a ducted tip hydrofoil to be at least 30% less for all positive angles of attack than that of a rounded tip hydrofoil. The hydrofoil that they tested was not geometrically similar to the one studied here, and therefore one could only hope for qualitative agreement between experiments and computations.

### **3.5 Conclusions**

The flow over two finite-span hydrofoils, one with a rounded tip and one with a ducted tip, was studied using the finite-volume flow solver CFD-ACE(U) from CFDRC. A k- $\epsilon$  turbulence model and a combination of C-H, H-H, tetrahedral and prism grids were used. Mesh sizes ranged from 350,000 - 550,000 cells. Cases were run with a second order accurate upwind scheme and the results compared to available experimental data. The aim of the study was to simulate the flow around a ducted tip hydrofoil with the hope of gaining a better understanding of the flow around the duct as well as providing a good basis for further optimization of the size and duct location on a propeller blade.

Grid dependence was studied for the rounded tip hydrofoil and it was shown that grid independence could be achieved for the majority of the flow. Near surface flow vector plots of the CFD-modelled hydrofoils at 7 and 12 degrees angle of attack were compared to SFV photographs from experiments done by Green (1988). Qualitatively, the overall agreement in flow directions along the hydrofoil is very good. Flow angles measured along the trailing edge of the different geometry hydrofoils suggest that the the ducted tip hydrofoil sheds less bound circulation over the majority of the wing span than does the rounded tip hydrofoil. This was confirmed by studying

the x-component of vorticity immediately downstream of the two hydrofoils, which showed that the vorticity is shed in the shape of a duct from the ducted tip hydrofoil instead of a concentrated circular vortex as is the case for the rounded tip hydrofoil. Also, the sectional lift along the span of the hydrofoils is higher for the ducted tip hydrofoil than for the rounded tip hydrofoil. The minimum pressure associated with the tip vortices is much lower for the rounded tip hydrofoil than the ducted tip hydrofoil, which is in agreement with experiments showing a reduced cavitation inception index for this geometry.

Future work will include continued use of CFD to optimize the duct size, shape and location on a propeller blade. This will be followed by experiments in a cavitation tunnel on a model propeller with ducted tips.

## CHAPTER 4 - CONCLUSIONS AND RECOMMENDATIONS FOR FUTURE WORK

### 4.1 Conclusions

The flow over ducted and rounded tip hydrofoils was studied using the finite-volume flow solver CFD-ACE(U) from CFD Research Corporation and a k- $\epsilon$  turbulence model. This research was motivated and based on experimental results of Green and Duan (1995) and Hordnes and Green (1998). They found that attaching a duct to a hydrofoil and a propeller blade suppresses the tip vortex rollup and results in reduced tip vortex cavitation without loss of efficiency. The idea with this research was to provide a good basis for computational optimization of duct location, size and shape on a propeller blade as well as advancing our understanding of the flow around a ducted tip hydrofoil. First the flow over two rounded tip hydrofoils was studied with validation in mind. This was followed by computations of the flow around a ducted tip hydrofoil. Key conclusions from these studies are the following:

1. Qualitatively, the surface flow of the rounded and ducted tip hydrofoils can be well predicted using the current numerical schemes and grids. A good overall agreement in flow pattern was achieved between the computational results and available experimental data on both ducted and rounded tip hydrofoils.
2. The pressure distribution can be very well predicted away from the tip. Close to the tip the vortex-induced suction minimum can be expected to be underpredicted. This is reflected in the computed sectional lift which was shown to be up to 12% lower than corresponding experimental data very close to the tip of a rounded tip hydrofoil. This differ-

ence is likely due to a combination of poor grid resolution, diffusion in the turbulence scheme and the low order differencing scheme.

3. The spanwise position of the trailing vortex can be very well predicted with the current scheme. The peak tangential velocity in the vortex core is well predicted but the total velocity can be somewhat underpredicted in the middle of the core.

4. The location of separation on the hydrofoils can be predicted quite accurately. This should be of great benefit for optimization studies of the ducted tip.

5. The trailing vorticity ( $x$ -component) from the ducted tip hydrofoil is shed in the shape of a duct instead of a concentrated circular vortex on the rounded tip hydrofoil. Previous researchers had speculated this to be the case, but it is here shown clearly. The ducted tip hydrofoil sheds less bound circulation over the majority of the wing span than does the rounded tip hydrofoil. This can also be concluded from the predicted lift along the span of the two hydrofoils, which is higher for the ducted tip hydrofoil.

## **4.2 Recommendations for Future Work**

It has become apparent throughout this work that it is, at this point in time, probably impossible to find through CFD the ultimate shape for a ducted tip propeller blade with the computational resources available. Each change to the shape of the duct normally requires a substantial amount of work - not only in changing the geometry but especially in gridding it. However, using CFD in combination with experiments will hopefully get us closer to an optimal shape for the ducted tip on a propeller. It is suggested that this "optimization" be done in the following steps.

1) Optimize the duct shape alone. Meshing the duct alone is a far more simple task and easier to run than a duct attached to a hydrofoil. The emphasis here should be to find a good smooth shape at the inlet that will reduce the chance of separation. The duct should be run at a range of angles of attack. It would also be of value to try different shapes of the duct aft of the inlet to optimize the lift gained from the duct.

2) Study the effect of different duct lengths, diameters and locations. This should preferably be done on a propeller blade since there is a difference in the incoming flow for a propeller blade and a hydrofoil. The hydrofoil experiences a constant spanwise, axial incoming flow, while the tip of the propeller sees a radially varying tangential incoming flow. If this proves unattainable on a propeller blade, doing this study on a hydrofoil should still provide important information.

3) Attach new “optimized” ducts to a model propeller for testing in a controlled environment.

## REFERENCES

- Abbott, I. H. and Von Doenhoff, A. E., 1959, "Theory of Wing Sections," Dover Publications, New York.
- Chahine, G.L., Frederick, G.F. and Bateman, R.D., 1993, "Propeller Tip Vortex Cavitation Suppression using Selective Polymer Injection," ASME Journal of Fluids Engineering, Vol. 115, pp. 497-503.
- Crump, S.F., 1948, "The Effects of Bulbous Blade Tips on the Development of Tip Vortex Cavitation on Model Marine Propellers", report C-99, David Taylor Naval Ship Research and Development Center.
- Dacles-Mariani, J., Zilliac G. G., Chow, J. S. and Bradshaw, P., 1995, "Numerical/Experimental Study of a Wingtip Vortex in the Near Field," AIAA Journal, Vol. 33, No. 9, pp. 1561-1568.
- Duan, S., 1995, "Analytical and Experimental Studies of Wing Tip Vortices," Ph.D. Thesis, University of British Columbia.
- Fruman, D.H. and Aflalo, S.S., 1989, "Tip Vortex Cavitation Inhibition by Drag Reducing Polymer Solutions," ASME Journal of Fluids Engineering, Vol. 111, pp. 211-216.
- Goodman, T.R. and Breslin, J.P., 1980, "Feasibility Study of the Effectiveness of Tip Sails on Propeller Performance", Report no. MA-RD-940-81006, Department of Ocean Engineering, Stevens Institute of Technology.
- Green, S.I., 1988, "Tip Vortices - Single Phase and Cavitating Flow Phenomena", Ph.D. Thesis, California Institute of Technology.
- Green, S.I., Acosta, A.J. and Akbar, R., 1988, "The Influence on Tip Geometry on Trailing Vortex Rollup and Cavitation Performance", ASME, Cavitation and Multiphase Flow Forum, pp. 76-80.
- Green, S.I., and Duan, S.Z., 1995, "The Ducted Tip - A Hydrofoil Tip Geometry with Superior Cavitation Performance," ASME Journal of Fluids Engineering, Vol. 117, pp. 665-672.
- Hordnes, I. and Green S. I., 1998, "Sea Trials of the Ducted Tip Propeller," ASME Journal of Fluids Engineering, Vol. 120, pp. 808-817.
- Hsiao, C. and Pauley, L. L., 1998, "Numerical Study of the Steady-State Tip Vortex Flow Over a Finite-Span Hydrofoil," ASME Journal of Fluids Engineering, Vol. 120, pp. 345-353.
- Hsiao, C. and Pauley, L. L., 1999, "Numerical Computation of Tip Vortex Flow Generated by a Marine Propeller," ASME Journal of Fluids Engineering, Vol. 121, pp. 638-645.

Itoh, S., Ishii, N., Tagori, T., and Ide, T., 1987, "Study of the Propeller with Small Blades on the Blade Tips (1<sup>st</sup> report)," Journal of the Society of Naval Architects of Japan, Vol. 159, pp. 82-90. Published in Japanese with English abstract.

Johnsson, C.A. and Rutgersson, O., 1991, "Leading Edge Roughness A Way to Improve Propeller Tip Vortex Cavitation," Propellers and Shafting Symposium , Paper no. 12.

Kroo, I., 2000, "Drag Due to Lift: Concepts for Prediction and Reduction," Annual Review of Fluid Mechanics, Vol 33, pp. 587-617.

Kroo, I., 2000, "Drag Due to Lift: Concepts for Prediction and Reduction," Annual Review of Fluid Mechanics, Vol. 33, pp. 587-617.

Kuipier, G., 1978, "Scale Effects on Propeller Cavitation Inception," 12th Symposium on Naval Hydrodynamics, Vol. 12.

McAlister, K. W., and Takahashi, R. K., 1991, "NACA 0015 Wing Pressure and Trailing Vortex Measurements," NASA Technical Paper 3151.

Mani, K., Sharma, S.D. and Arakeri, V.H., 1988, "Effect on Propeller Blade Modification and Cavitation Induced Noise," ASME FED Vol. 64, pp. 64-67.

Platzer, G.P. and Souders, W.G., 1979, "Tip Vortex Cavitation Delay with Application to Marine Lifting Surfaces. A Literature Survey," Report no. 79/051, David Taylor Naval Ship Research and Development Center.

[www.cfdrc.com](http://www.cfdrc.com)

## APPENDIX 1 - SIMULATION ON A 2D HYDROFOIL

This appendix contains results from simulations run on a two dimensional hydrofoil with a NACA 0012 airfoil geometry. The 2D simulations were run to provide some base knowledge for the number of cells and grid distribution required to predict the flow behavior reasonably well before extending the hydrofoil into the third dimension. The simulations were all run at  $Re = 9 \times 10^6$  and the flow domain around the hydrofoil was gridded with a C-mesh. The flow domain extended 5 chord lengths behind the trailing edge of the hydrofoil and 5 chord lengths above and below the hydrofoil. The flow inlet (which had the form of a C) reached 5 chord lengths in front of the leading edge of the hydrofoil. The foil was tilted around its quarter chord point when run at an angle relative to the freestream flow. The pressure-based, finite-volume flow solver CFD-ACE(U) from CFDRC was used for the simulations and cases were run with a  $k-\epsilon$  turbulence model and a second-order accurate upwind differencing scheme. The boundary conditions were as shown in Figure A.1.1.

The primary grid used in the 2D study had a total of 5740 cells with the first cell spacing at the hydrofoil surface specified as 0.00015 chord lengths (c). A convergence study was performed to evaluate the effects of mesh size and local density near the hydrofoil. 3 simulations were run with 3 different meshes with the hydrofoils tilted at  $\alpha = 10^\circ$  angle of attack. The basic features of the 3 different meshes are listed in Table A.1.1. Mesh 2 is the primary grid. Mesh 1 had approximately half of the number of grid points on each edge as that of Mesh 2, resulting in about 4 times fewer cells. Mesh 3 had twice the number of grid points on each edge as that of Mesh 2, resulting in 4 times more cells. It should be noted that the reason that the first cell spac-

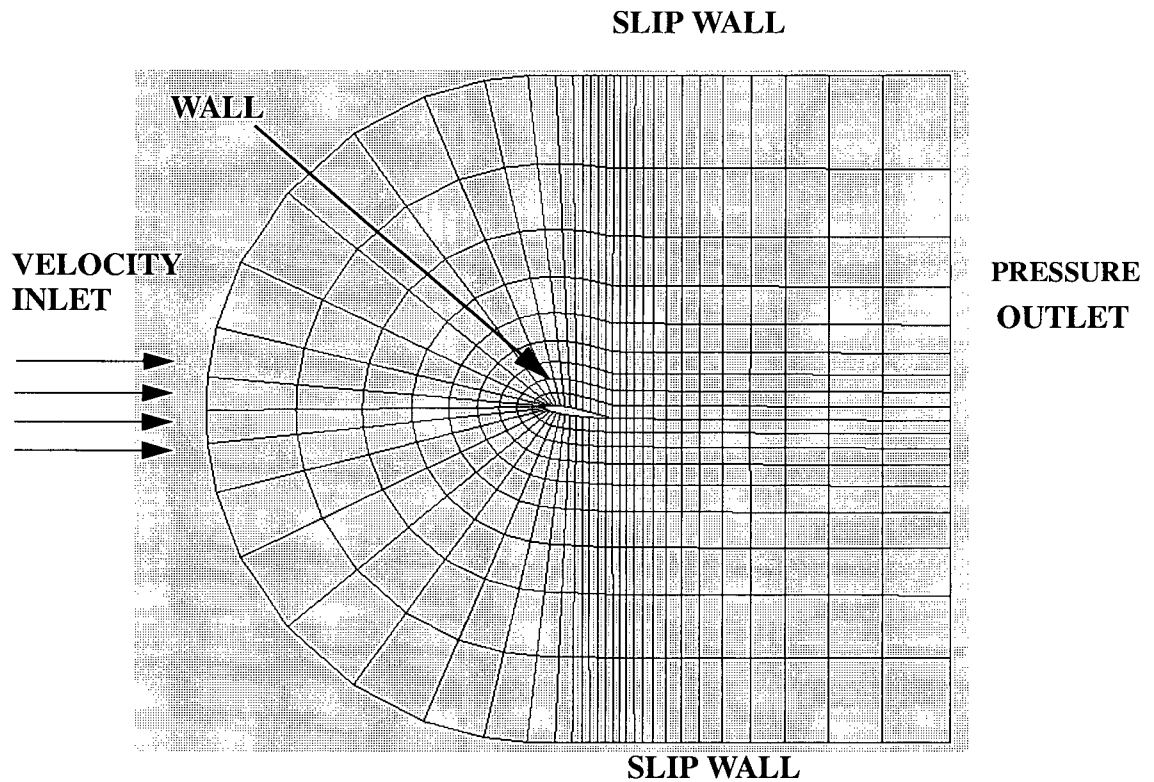


Figure A.1.1 Grid shape and boundary conditions for modeling of 2D hydrofoil.

Table A.1.1 Mesh Distribution for Convergence Study

	Mesh 1	Mesh 2	Mesh 3
Nr. of grid points on hydrofoil	51	101	201
Nr. of remaining grid points in streamwise direction	21	41	81
Nr. of grid points in surface normal direction	21	42	83
Total number of cells	1400	5740	22960
First cell spacing	0.0006c	0.00015c	0.00015c
Approximate $y^+$ value in first cell	~ 80-150	~ 20	~ 20

ing was not reduced for Mesh 3 from that of Mesh 2 is that further reduction in the first cell spacing resulted in divergence.

Lift and drag coefficients ( $C_D$  and  $C_L$ ) were computed for Mesh 1, Mesh 2 and Mesh 3 and compared to the experimental results of Abbott and Doenhoff (1959). As may be seen in Table A.1.2. there is great change in both lift and drag coefficients between Mesh 1 and Mesh 2 but less than 1% change in lift and 5% change in the drag coefficient between Mesh 2 and 3. Although Mesh 2 doesn't seem to give completely grid converged results it was decided to run the remaining simulations with grids that had the same distribution as Mesh 2. This decision was made because it would have been computationally prohibitive, with the equipment available, to run three dimensional cases with e.g. as many cells as Mesh 3 in these two dimensions, if the flow domain in the third dimension (spanwise) also was to be resolved well. Also, although the change in drag between the two grids is 5%, the predicted drag coefficient based on Mesh 3 is still approximately 60% higher than the experimental drag coefficient and thus improvement between Mesh 2 and Mesh 3 is in fact very little relative to both meshes' deviation from the experimental results.

**Table A.1.2 Convergence Study - Lift and Drag Coefficients**

	$C_L$	$C_D$
Mesh 1	0.88	0.04
Mesh 2	1.06	0.020
Mesh 3	1.07	0.019
Experimental Results	1.08	0.012

Following the grid convergence study, the hydrofoil with the grid distribution of Mesh 2 was run at several different angles of attack and the computed lift and drag coefficients compared to experimental data (Figures A.1.2 and A.1.3.). The computed lift compares very well with

experimental data and the difference between computed and experimental lift coefficients is always less than +/- 0.03. The computed drag is however not as promising despite showing a similar trend as the experimental drag. The difference is least at low angles of attack but the computed drag escalates to approximately 60% more than the experimental drag at  $\alpha = 10^\circ$ . This can be attributed in part to poor resolution of the boundary layer. The standard k- $\epsilon$  model used for these simulations is a high Reynolds number model and is not intended to be used in the near-wall regions where viscous effects dominate the effects of turbulence. Instead, wall functions are used in the turbulence model in cells adjacent to the walls. Resolving the boundary layer further, however, resulted, as mentioned before, in divergence of the simulation. It is recommended in the CFDRC manuals ([www.cfdrc.com](http://www.cfdrc.com)) that the first cell spacing be at  $y^+ > 11.5$  when using the k- $\epsilon$  model to avoid divergence of simulations and the divergence thus came as no surprise.

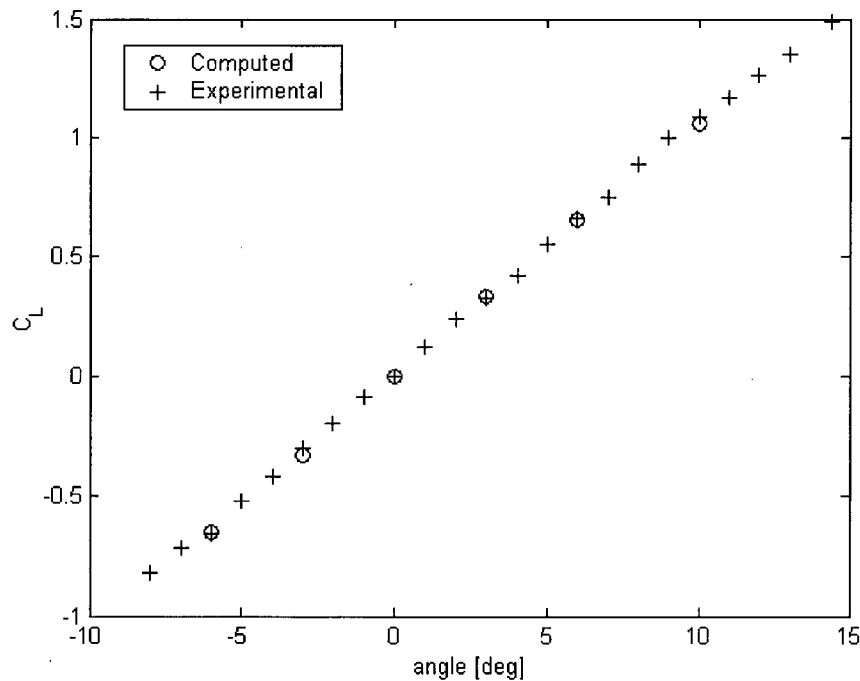


Figure A.1.2 Lift coefficients as a function of angle of attack at  $Re = 9.0 \times 10^6$ .

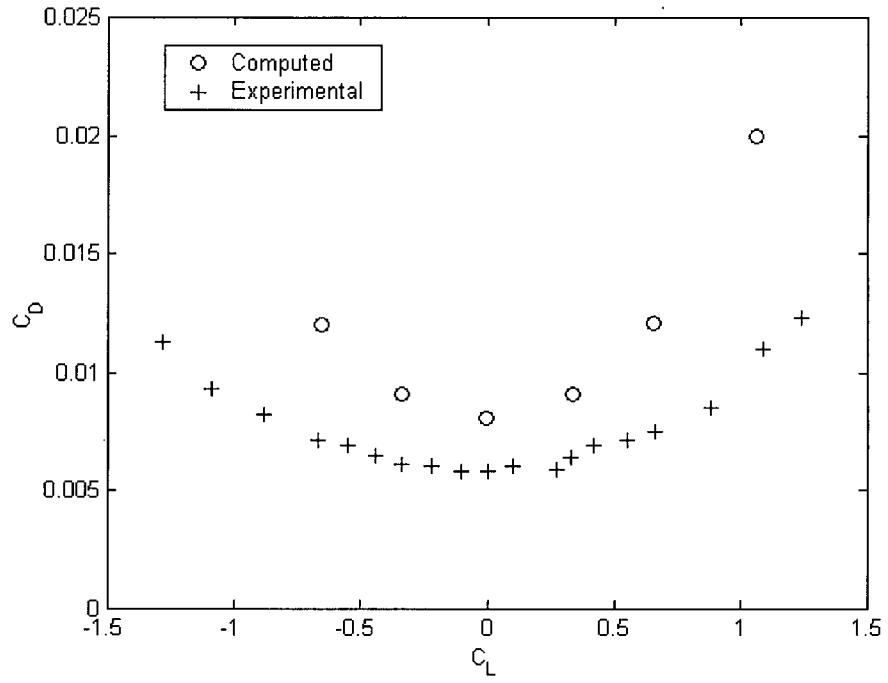
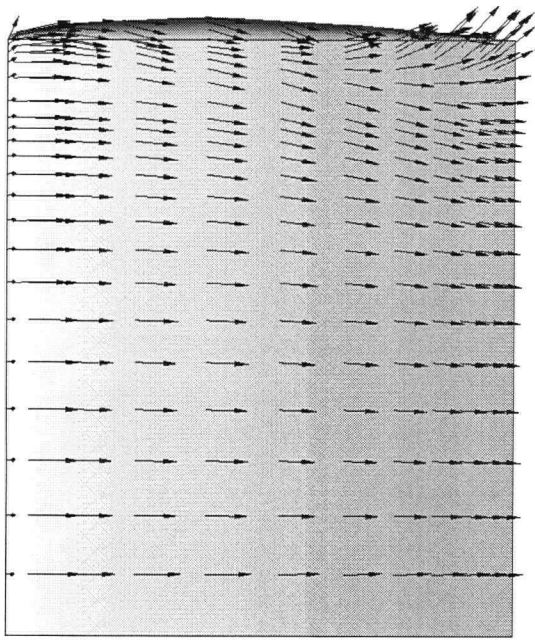


Figure A.1.3 Drag coefficients as a function of lift coefficient at  $Re = 9.0 \times 10^6$ .

## **APPENDIX 2 - SURFACE VECTOR PICTURES AND SFV PHOTOGRAPHS AT $\alpha = 7^\circ$**

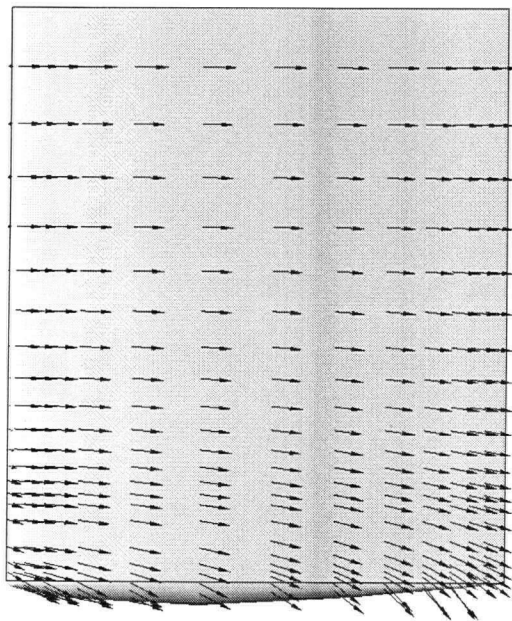
This appendix contains surface vector pictures of the rounded and ducted tip hydrofoils as well as SFV photographs by Green (1988) at  $\alpha = 7^\circ$ . The hydrofoils, their computational domains, and the flow properties of the surrounding fluid are those described in Chapter 3.



(a)

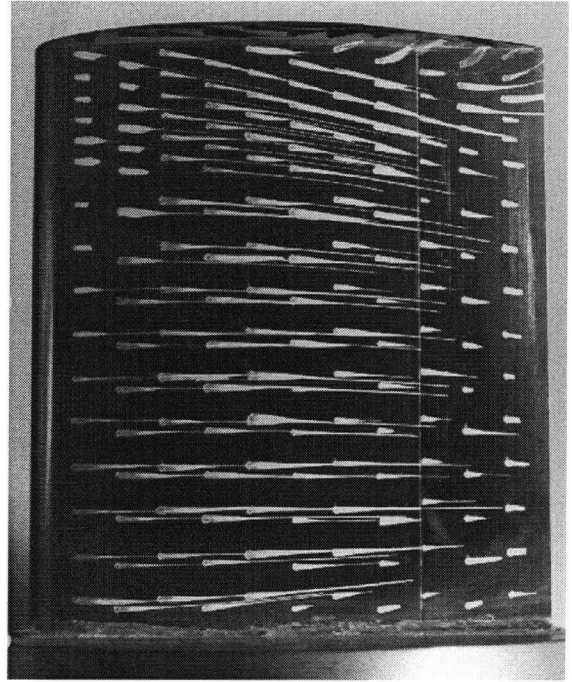


(b)



(c)

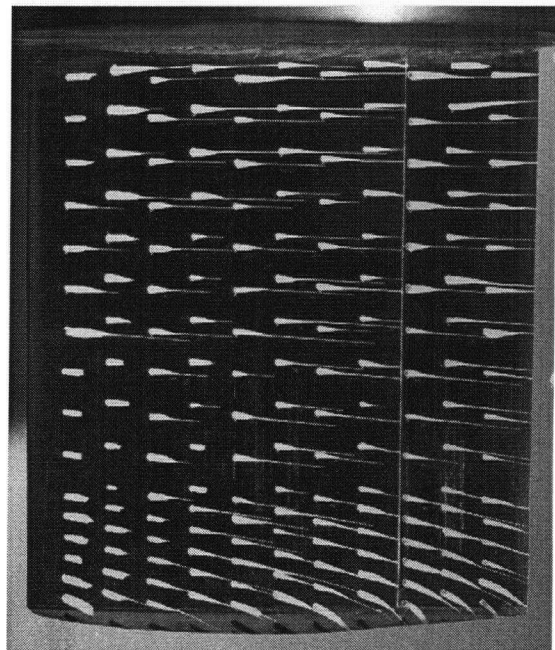
Figure A.2.1 Surface vector pictures of the (a) suction side, (b) tip and (c) pressure side of the rounded tip hydrofoil at  $\alpha = 7^\circ$ .



(a)

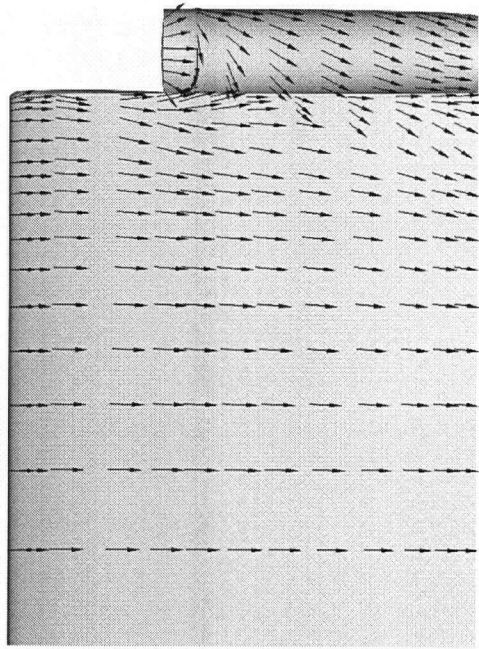


(b)

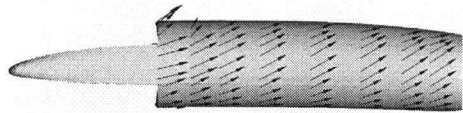


(c)

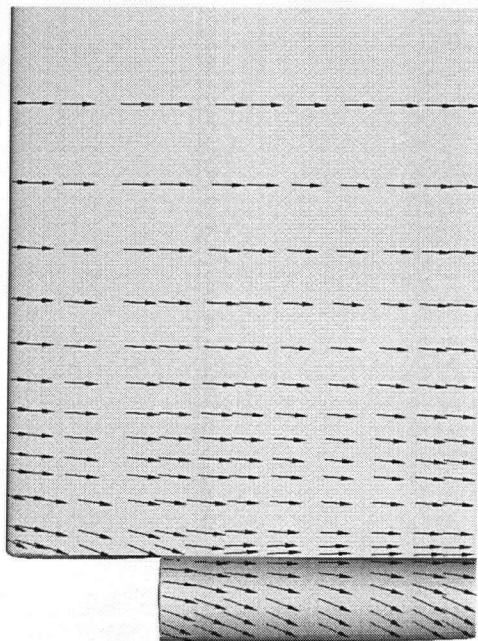
Figure A.2.2 SFV photographs of the (a) suction side, (b) tip and (c) pressure side of the rounded tip hydrofoil at  $\alpha = 7^\circ$ .



(a)

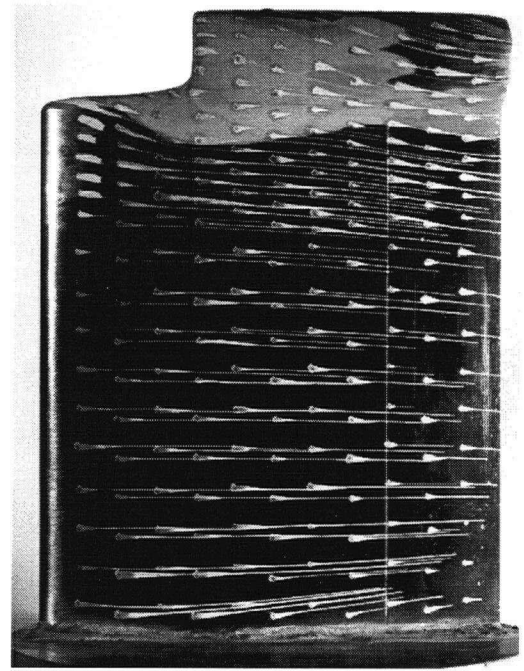


(b)

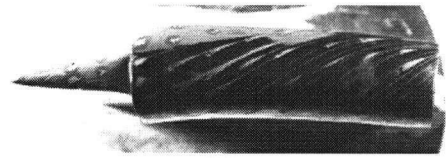


(c)

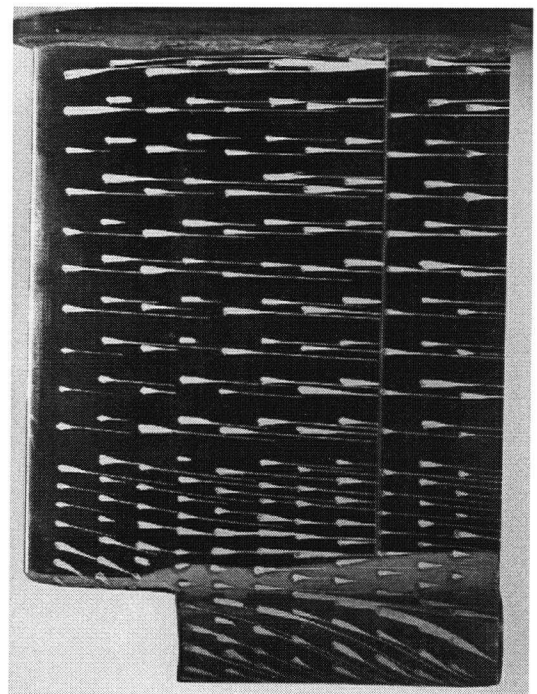
Figure A.2.3 Surface vector pictures of the (a) suction side, (b) tip and (c) pressure side of the ducted tip hydrofoil at  $\alpha = 7^\circ$ .



(a)



(b)



(c)

Figure A.2.4 SFV photographs of the (a) suction side, (b) tip and (c) pressure side of the ducted tip hydrofoil at  $\alpha = 7^\circ$ .

## APPENDIX 3 - LIFT ON THE ROUNDED AND DUCTED TIP HYDRO-FOILS

This appendix contains excess lift data from the simulations discussed in Chapter 3. The lift coefficients ( $C_L$ ) are calculated by CFD-ACE(U) by integrating the pressure over the x-z plane of the hydrofoil. The calculated coefficients are displayed in Table A.3.1 and are all based on the planform area of the rounded tip hydrofoil.

**Table A.3.1 Lift Coefficients for the Rounded and Ducted Tip Hydrofoils**

	Rounded Tip 7°	Ducted Tip 7°	Rounded Tip 12°	Ducted Tip 12°
$C_L$	0.5434	0.6655	0.8588	0.9491

It is clear from the table that the ducted tip hydrofoil produces more lift than the rounded tip one. It should however be observed that since all the lift coefficients are based on the planform area of the rounded tip hydrofoil, the extra surface area provided by the duct is not taken into account. In table A.3.2 the ducted tip hydrofoil lift coefficients have been recalculated based on the planform area of the ducted tip hydrofoil, including the duct itself.

**Table A.3.2 Lift Coefficients for the Rounded and Ducted Tip Hydrofoils - Modified**

	Rounded Tip 7°	Ducted Tip 7°	Rounded Tip 12°	Ducted Tip 12°
$C_L$	0.5434	0.6008	0.8588	0.8643

According to these calculations, the lift coefficients at  $\alpha = 7^\circ$  are within 10% and  $\alpha = 12^\circ$  within 1% of each other. This agrees fairly well with the experimental findings of Duan (1995), given the different geometry hydrofoils he used. He measured the lift on ducted and rounded tip hydrofoils of similar cross section (66-209) but the duct was 0.096 chordlengths (c) in diameter,

and the hydrofoils had aspect ratios (based on semi-span) of 1.15 - 1.165 versus the diameter of 0.19c and aspect ratio of 1.17 used in the present computations. Duan found that if he accounted for the difference in planform areas of the rounded and ducted tip hydrofoils in his calculations, the lift coefficients for the two geometries were identical to within experimental error. This applied for all of the angles measured, which ranged from  $\alpha = 6^\circ$  to  $\alpha = 17^\circ$ .

It was already shown in Chapter 3 that the ducted tip hydrofoil generates greater lift along its span (before the duct) than the corresponding rounded tip hydrofoil at  $\alpha = 12^\circ$ . In Figure A.3.1 the sectional lift coefficients ( $C_L$ ) at  $\alpha = 12^\circ$  are shown. The lower lift for the ducted tip hydrofoil seen close to the wing root (Figure A.3.2) is due to separation at the leading edge which was described in Chapter 3.

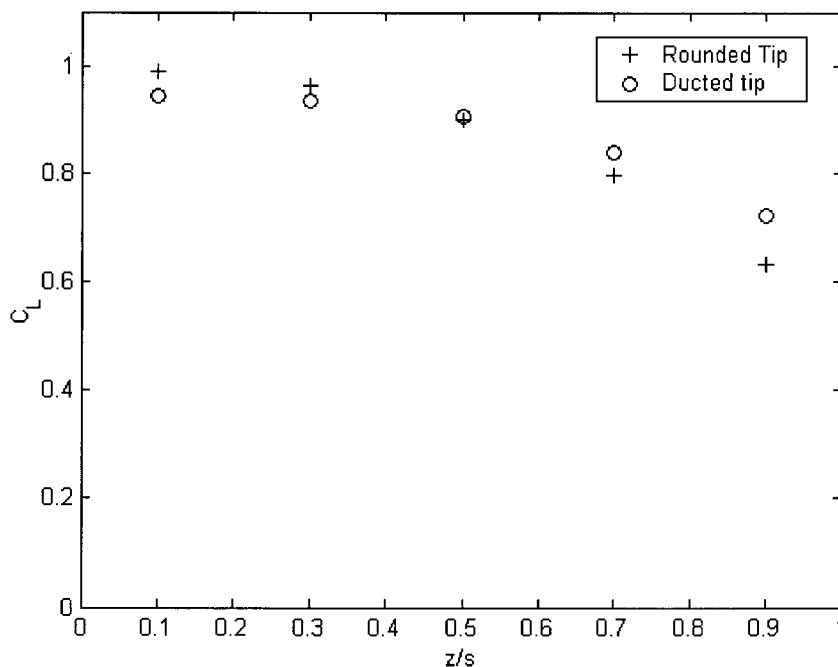


Figure A.3.1 Sectional lift along spanwise stations of the hydrofoils at  $\alpha = 12^\circ$ .